ORIGINAL RESEARCH

Cardiomyocyte Functional Etiology in Heart Failure With Preserved Ejection Fraction Is Distinctive—A New Preclinical Model

Claire L. Curl, PhD; Vennetia R. Danes, MD, PhD; James R. Bell, PhD; Antonia J. A. Raaijmakers, MSc; Wendy T. K. Ip, PhD; Chanchal Chandramouli, PhD; Tristan W. Harding, MD; Enzo R. Porrello, PhD; Jeffrey R. Erickson, PhD; Fadi J. Charchar, PhD; Andrew R. Kompa, PhD; Amanda J. Edgley, PhD; David J. Crossman, PhD; Christian Soeller, PhD; Kimberley M. Mellor, PhD; Jonathan M. Kalman, MD; Stephen B. Harrap, MD, PhD; Lea M. D. Delbridge, PhD

***Background*—**Among the growing numbers of patients with heart failure, up to one half have heart failure with preserved ejection fraction (HFpEF). The lack of effective treatments for HFpEF is a substantial and escalating unmet clinical need—and the lack of HFpEF-specific animal models represents a major preclinical barrier in advancing understanding of HFpEF. As established treatments for heart failure with reduced ejection fraction (HFrEF) have proven ineffective for HFpEF, the contention that the intrinsic cardiomyocyte phenotype is distinct in these 2 conditions requires consideration. Our goal was to validate and characterize a new rodent model of HFpEF, undertaking longitudinal investigations to delineate the associated cardiac and cardiomyocyte pathophysiology.

***Methods and Results*—**The selectively inbred Hypertrophic Heart Rat (HHR) strain exhibits adult cardiac enlargement (without hypertension) and premature death (40% mortality at 50 weeks) compared to its control strain, the normal heart rat. Hypertrophy was characterized in vivo by maintained systolic parameters (ejection fraction at 85%–90% control) with marked diastolic dysfunction (increased E/E′). Surprisingly, HHR cardiomyocytes were hypercontractile, exhibiting high Ca^{2+} operational levels and markedly increased L-type Ca^{2+} channel current. In HHR, prominent regions of reparative fibrosis in the left ventricle free wall adjacent to the interventricular septum were observed.

***Conclusions*—**Thus, the cardiomyocyte remodeling process in the etiology of this HFpEF model contrasts dramatically with the suppressed Ca^{2+} cycling state that typifies heart failure with reduced ejection fraction. These findings may explain clinical observations, that treatments considered appropriate for heart failure with reduced ejection fraction are of little benefit for HFpEF—and suggest a basis for new therapeutic strategies. **(*J Am Heart Assoc*. 2018;7:e007451. DOI: 10.1161/JAHA.117.007451.)**

Key Words: calcium handling • cardiac • cardiomyocyte • fibrosis • heart failure preserved ejection fraction • hypertrophy

Among the growing numbers of patients with heart failure, as many as one half have heart failure with preserved ejection fraction (HFpEF), and clinical trials have yet to define an effective and specific treatment for this condition.[1,2] The pathophysiology of HFpEF is characterized by near normal systolic function coincident with diastolic dysfunction and inadequate ventricular filling at normal pressures. Surprisingly, while there has been considerable focus on refining

---

From the Departments of Physiology (C.L.C., V.R.D., J.R.B., A.J.A.R., W.T.K.I., C.C., T.W.H., E.R.P., K.M.M., S.B.H., L.M.D.D.) and Medicine (J.M.K.), University of Melbourne, Victoria, Australia; Murdoch Children's Research Institute, Melbourne, Australia (E.R.P.); Department of Physiology, University of Otago, Dunedin, New Zealand (J.R.E.); School of Applied & Biomedical Sciences, Federation University, Ballarat, Australia (F.J.C.); Department of Medicine, St. Vincent's Hospital, The University of Melbourne, Australia (A.R.K., A.J.E.); Department of Physiology, University of Auckland, New Zealand (D.J.C.); Biomedical Physics, University of Exeter, United Kingdom (C.S.).

Accompanying Data S1, Tables S1 through S3, and Figures S1 through S9 are available at http://jaha.ahajournals.org/content/7/11/e007451/DC1/embed/inline-supplementary-material-1.pdf

These data were presented at the Symposium of the Basic Cardiovascular Sciences Council (BCVS) of the American Heart Association, July 10 to 13, 2017, in Portland, OR.

Correspondence to: Lea M. D. Delbridge, PhD, Cardiac Phenomics Laboratory, Department of Physiology, University of Melbourne, Victoria, Australia 3010. E-mail: lmd@unimelb.edu.au

Received September 7, 2017; accepted April 18, 2018.

Clinical Perspective

What Is New?

- Heart failure with preserved ejection fraction (HFpEF) is a condition for which there is no specific treatment.
- The lack of HFpEF-specific animal models represents a major preclinical barrier in advancing understanding of HFpEF.
- We validate and characterize a new rodent model of HFpEF, undertaking longitudinal investigations to delineate the associated cardiac and cardiomyocyte pathophysiology.
- Surprisingly, HHR cardiomyocytes were hypercontractile, exhibiting high Ca^{2+} operational levels and markedly increased L-type Ca^{2+} channel current.

What Are the Clinical Implications?

- The cardiomyocyte remodeling process in the etiology of this HFpEF model contrasts dramatically with the suppressed Ca^{2+} cycling state that typifies heart failure with reduced ejection fraction.
- These findings may explain clinical observations that treatments considered appropriate for heart failure with reduced ejection fraction are of little benefit for HFpEF—and suggest a basis for new therapeutic strategies.

differential diagnostic criteria for HFpEF relative to heart failure with reduced ejection fraction (HFrEF), an understanding of the cardiomyocyte functional phenotype that characterizes HFpEF is lacking. The lack of HFpEF-specific animal models represents a major preclinical barrier in advancing understanding of HFpEF.[3] Defining the cellular basis of HFpEF dysfunction is critical for guiding the development of new treatments for this failure condition.[4]

Although the HFpEF phenotype is not homogenous,[2,5,6] cardiac hypertrophy is considered an important diagnostic element, and the extent of hypertrophy is a key prognostic indicator in HFpEF.[7,8] Hypertension (although often present as a comorbidity to a variable extent in different HFpEF populations) has not been identified as a baseline discriminator in determining the development of HFpEF in outcome trials.[9] In addition to hypertrophy, heart failure guidelines also recognize other diagnostic features of HFpEF, including increased left ventricular filling pressures, normal left ventricular end-diastolic volume, and fibrosis.[7,8,10] Systemic inflammatory involvement and metabolic disturbances linked with comorbidities may also contribute.[9]

In HFrEF, the cellular “remodeling” processes generally understood to characterize the progression to failure include reduced cardiomyocyte contractile response, diminished systolic Ca^{2+} activator availability, and dysregulated sarcoplasmic reticulum (SR) Ca^{2+} store operation.[11] This general etiology is inferred primarily from experimental observation of tissues and myocytes of various animal models of systolic dysfunction occurring as a result of abnormal volume or pressure loads and some studies of end-stage failing human myocardium.[12] Cell-directed treatments for HFrEF have principally focused on interventions to augment availability or actions of cardiomyocyte activator Ca^{2+}.[13] These HFrEF therapies, which have largely relied on neurohumoral approaches involving angiotensin, aldosterone, and β-adrenoceptor targets, have not been successful in the HFpEF context,[3,14] raising questions about the cardiomyocyte phenotypes in HFpEF.

There is a poor understanding of the cardiomyocyte pathophysiology of HFpEF, in large part because of the limited availability of appropriate HFpEF preclinical models. Indeed, this problematic lack of animal models has recently been highlighted as a major barrier in the progression of preclinical mechanistic work available to inform new therapeutic directions for HFpEF.[3] Proposed models generally involve pressure overload interventions, with secondary development of diastolic dysfunction, and do not fully recapitulate clinical features.[15] The cardiomyocyte HFpEF functional characteristics, wherein the intrinsic pathologic trigger is not a systolic loading challenge, could be expected to be very different from the HFrEF myocyte phenotype. There are no studies of intact HFpEF-derived cardiomyocytes (human or animal) from disease settings involving primary cardiac pathology. Findings from membrane disrupted cell preparations derived from the myocardium of patients with diastolic heart failure have described sarcomeric structures exhibiting increased passive force response to stretch—but there has been no investigation of intact cardiomyocyte Ca^{2+} handling and contractile responsiveness in the HFpEF setting arising from underlying myocardial hypertrophic pathogenesis.

Here, we report and validate a novel rodent model of HFpEF—which exhibits cardiac hypertrophy and premature mortality independent of hemodynamic loading.[16,17] In the hypertrophic heart rat strain (HHR), we demonstrate that the in vivo progression to diastolic failure (with preservation of systolic performance) is accompanied by unexpected hyperfunction of cardiomyocytes with elevated systolic activator Ca^{2+} availability and contractile response. Molecular and electrophysiologic analyses identify arrhythmogenic cellular substrates. Thus, the cardiomyocyte remodeling process in the etiology of this HFpEF model contrasts dramatically with that seen in the HFrEF state. These findings may explain clinical observations that intervention strategies considered appropriate for HFrEF are of little benefit for HFpEF. New insights from our unique animal model of HFpEF provide opportunities to develop novel and targeted HFpEF therapeutic approaches.

Methods

The data, analytic methods, and study materials will be made available to other researchers for purposes of reproducing the results or replicating the procedure on reasonable request.

Detailed methods are available in Data S1.

Experimental Animals

A novel normotensive, hypertrophic rat strain generated through selection and cross breeding of Fischer 344 and spontaneously hypertensive rat strain progenitors has previously been described.[16,17] Briefly, initial spontaneously hypertensive rat genomic analysis had identified blood pressure–independent, hypertrophic genetic loci.[18] Selection for large and small echocardiographic heart size and low blood pressure was used to derive simultaneously the hypertrophic heart rat (HHR) and its control, the normal heart rat (NHR), respectively,[16] now beyond the F50 generation of inbreeding. The HHR constitutes a polygenic model of spontaneous cardiac hypertrophy with a natural disease history. Experiments were performed using male HHR and NHR at the failure and prefailure ages specified below. Normotension in HHR and NHR has been demonstrated previously,[16] and here equivalent diurnal mean arterial pressures were confirmed telemetrically (Figure S1A).

All experimental animals were housed under a 12-hour light/dark cycle with water and standard chow provided ad libitum. All investigations were undertaken in accordance with the National Health and Medical Research Council/Commonwealth Scientific and Industrial Research Organisation/ACC Australian Code of Practice for the Care and Use of Animals for Scientific Purposes (1997), as approved (University of Melbourne Animal Ethics Committee).

Echocardiography, Electrocardiography, and Hemodynamic Measurements

Echo- and electrocardiography were performed under light anesthesia (inhalation of isoflurane at 1.5%). Cardiac structure and systolic and diastolic function were evaluated by transthoracic 2-dimensional B- and M-mode and blood flow and tissue Doppler echocardiography (GE Vivid 9; 15 mHz i13L linear array transducer). Acquisition and offline analysis was performed with GE EchoPac software. ECGs were obtained using external clip leads in standard configuration. Ambulatory 24-hour blood pressure measurements were made using implanted devices to record from the intra-abdominal aorta (TA11PA-C40, DSI). To perform left ventricular catheterization, animals were anesthetized with sodium pentobarbital (60 mg/kg), intubated and ventilated, and a 2F miniaturized combined conductance catheter-micromanometer (Model SPR-838 Millar instruments, Houston, TX) was inserted into the right carotid and advanced into the left ventricle until stable pressure-volume loops were obtained. Data were acquired under steady-state conditions and during preload reduction.

Using the pressure conductance data, a range of functional parameters was then calculated including end-diastolic pressure, maximum rate of pressure change in the ventricle (+dP/dt max), minimum rate of pressure change in the ventricle (−dP/dt min) and the slope of the end-diastolic pressure volume relationship.

Histologic Analysis of Myocardial Collagen Content and Confocal Analysis of Cardiomyocyte Ultrastructure

To evaluate collagen histology, hearts were fixed in 10% formalin for histologic analysis using picrosirius red as previously described.[19] Images were captured with brightfield microscopy using the Zeiss Imager D1, connected to a Zeiss AxioCam MRc5 color camera and using AxioVision 40 version 4.7.1.0 acquisition software (Zeiss, Germany) with 10 images per section, from 2 sections per heart. Image analysis was performed using Image Pro Plus (V4.5.1, Media Cybernetics, Bethesda, MD) in a "blinded" manner. For ultrastructural analysis to examine cardiomyocyte sarcomeric integrity, high-resolution confocal microscopy was performed on fixed tissues labeled with the fluorescent marker wheat germ agglutinin to delineate cardiomyocyte T-tubule geometry using a Zeiss LSM410 confocal microscope and ×63 NA 1.25 oil-immersion objective. The t-tubule images were converted to frequency space using fast Fourier transform, and the peak in the power spectrum corresponding to the sarcomere spacing was estimated by Gaussian fit ("T power").

Cell Isolation and Cardiomyocyte Morphology

NHR and HHR single ventricular myocytes were isolated enzymatically using methods previously described.[19,20] Briefly, hearts were removed and perfused retrogradely on a Langendorff apparatus with Ca^{2+}-free bicarbonate-buffered physiologic saline solution, maintained at 37°C, with the following composition (mmol/L): NaCl, 118; KCl, 4.8; KH_2PO_4, 1.2; $MgSO_4$, 1.2; $NaHCO_3$, 25, glucose, 11. Following 20 minutes of 0.45 mg/mL collagenase (Worthington, Type II) perfusion, hearts were removed from the perfusion apparatus, the left ventricle was isolated and placed in a conical flask, and myocytes were dispersed by gentle agitation. Fractions containing viable cells were resuspended at room temperature in 2 to 3 mL of HEPES-buffered physiologic saline containing 1 mmol/L Ca^{2+} and were stored at room temperature. Cells were used within 8 hours.

Whole-Cell Patch Clamp

Voltage-gated Ca^{2+} currents (I-Ca) and Na^{+}/Ca^{2+} current (I-NCX) were measured using a whole-cell voltage clamp (Axopatch 200B, Digidata 1200B, Axon Instruments) with 1 to 3 MΩ pipette resistances (TW150F-3, World Precision Instruments). For I_{Ca}, voltage step protocols with 3 holding potentials were applied: −115, −90, and −50 mV. For I_{NCX}, a combined voltage step and ramp protocol from holding potential −90 mV to −45 mV to 0 mV to +80 mV to −140 mV was implemented. Current analysis procedures were performed using Clampfit (pClamp8).

Cardiomyocyte Intracellular Ca^{2+} and Contractility Measurements

Intracellular Ca^{2+} and cell length were measured simultaneously by microfluorimetry and edge detection (IonOptix). Cells were fura-2/AM-loaded (2.5 μmol/L, 20 minutes, Molecular Probes), superfused with HEPES-Krebs buffer and field stimulated. Cardiomyocyte performance was evaluated under basal paced conditions (37°C, 3 Hz, 1.5 mmol/L Ca^{2+}), during a rest interval (37°C, 1.5 mmol/L Ca^{2+} 3 Hz for 5 minutes, stimulator off 30 seconds), with different inotropic challenges (4 mmol/L Ca^{2+}, isoproterenol 10^{-8} mol/L and in response to rapid caffeine spritz to evaluate SR load (Ca^{2+} transient only).

Immunoblotting

Left ventricular tissue was homogenized and nonfractionated homogenates were reconstituted in sodium dodecylsulphate sample buffer. Equal volumes were loaded onto polyacrylamide gels for electrophoresis and immunoblot analysis. Antibody usage is tabulated in Figure S2A.

Statistical Analyses

In general (unless otherwise stated) data are presented as mean±SEM. Comparisons between two groups with normally distributed data were performed with Student unpaired *t* test. Data from experiments with two groups assessed at multiple points were evaluated by a one-way ANOVA with repeated measures. Two-way ANOVA was used for evaluation of data groups comprising 2 factors. Correlation analyses were performed to determine the Pearson coefficient within each strain and significance values evaluated. Data are shown depicting linear regression plots for each strain (SPSS c21.0; Graph Pad Prism V6). Data analysis was performed in a blinded manner. Survival (Kaplan–Meier) data were analyzed by log-rank Mantel-Cox test. Differences were considered significant at $P<0.05$ (SPSS v.21.0; Graph Pad Prism V6).

Results

Premature Mortality, Hypertrophy, and Diastolic Dysfunction With Preserved Systolic Function in the HHR

HHR and NHR cohorts were tracked longitudinally to characterize the functional and structural development and consequences of hypertrophy. HHRs died prematurely (primary end point) with a 40% mortality by 50 weeks of age compared with 0% NHR mortality (Figure 1A). Of those animals aged to end point or requiring euthanasia due to acute symptomatic deterioration, ≈40% exhibited pulmonary edema (lung weight index HHR 5.69±0.8 versus NHR 3.75±0.1, $P<0.05$). Other animals exhibited sudden premature death. Cardiac weight index at autopsy was substantially elevated (Figure 1B). In vivo function and structure was measured by echocardiography at 50 weeks (cohort surviving) and at 30 weeks (full cohort). Hemodynamic measures using cardiac catheterization were also obtained from a cohort of 50-week animals (Table S1, Figure S1B and S1C). HHR ejection fraction was substantially preserved at 85% to 90% NHR level at 50 and 30 weeks, respectively (Figure 1C and 1D, Table S1). While these 10% to 15% differences could be resolved statistically, the systolic performance levels could be considered to be relatively preserved. In the clinical setting, the maintenance of ejection fraction at 85% to 90% of normal value would be identified as "preserved" and considered a diagnostic element in establishing HFpEF occurrence. Maintained systolic function in HHRs was evident in the absence of significant dilation (diastolic chamber dimension), while systolic chamber dimension changes matched ejection fraction maintenance at 85% to 90% NHR value (Figure 1E, Table S1). Diastolic dysfunction at 30 and 50 weeks was evident in HHRs with markedly elevated E/E' (Figure 1F, Table S1) which was consistent with significantly increased end-diastolic pressure-volume relationship measurement from pressure-volume loop analysis (Figure S1B and S1C). HHR tachycardia was apparent, consistent with progression to failure (Figure 1G, Table S1). Thus, HHRs exhibited premature mortality, preserved ejection fraction, and substantially degraded diastolic performance relative to controls (ie, HFpEF). Interestingly, evaluation of very young HHR cohorts showed the emergence of diastolic dysfunction early, with maximal systolic function (Figure S3).

Histologic analyses in the 50-week HHRs revealed the presence of dispersed focal fibrotic areas in the extracellular matrix that did not follow a typical perivascular localization. The regions of most prominent occurrence of fibrotic foci were mapped to the transverse midwall area of the left ventricle adjacent to the interventricular septum and the area of septal free wall confluence (Figure S4). Although the overall fibrotic load in HHR was significantly greater than NHR

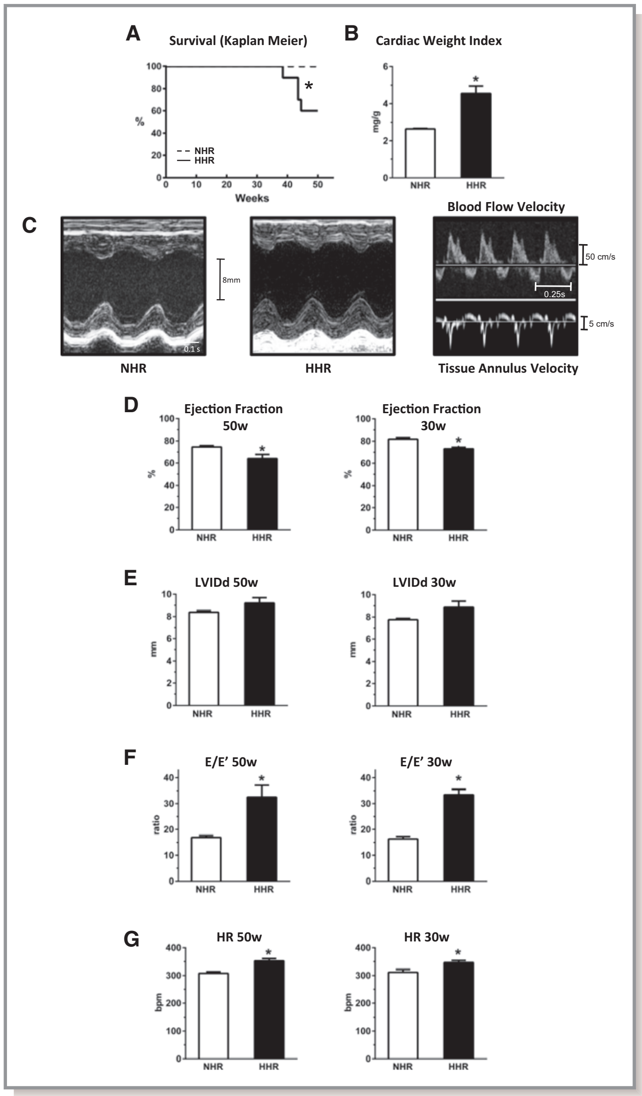

Figure 1. Premature mortality, hypertrophy, and diastolic dysfunction with preserved systolic function in the hypertrophic heart rat (end point age 50 weeks, prefailure 30 weeks). A, Survival, normal heart rat (NHR, dashed line) and hypertrophic heart rat (HHR, solid line). B, Postmortem cardiac weight index (mg/g). (50 weeks). C, Exemplar M-mode echocardiographs HHR vs NHR hearts, and exemplar blood flow and tissue Doppler images (50 weeks). D, Preserved systolic function in HHR with minimal decrement of ejection fraction (EF). E, Left ventricular internal diameter (diastole) (LVIDd). F, Diastolic function—E/E′. G, Heart rate (HR, bpm). Graphs show mean ± SEM. For A, $*P=0.0004$ (log-rank Mantel-Cox test), for B and D through G, $*P<0.05$ (Student *t* test, n=6–10 hearts/group).

(Figure 2A through 2E), when focal areas were excluded, the interstitial matrix histology was similar in HHRs and NHRs. Thus, this failure-associated histology comprised focal fibrotic regions indicative of localized reparative responses.

Progression to failure has been linked with loss of cardiomyocyte T-tubule structural integrity, understood to compromise excitation-contraction coupling efficacy. Despite the very marked cardiomyocyte size increase, ultrastructural analyses found no evidence of T-tubule structural disturbance in HHR myocytes. Morphologically, there was no evidence of T-tubule spatial dispersion. The wheat germ agglutinin–stained myocytes were similar for HHRs and NHRs, confirming the absence of significant changes in the T-system morphology (Figure 2F through 2I).

Cardiomyocyte Hypercontractility Characterizes Progression to Failure With Preserved Systolic Function

Electromechanical performance of fura-2 loaded isolated cardiomyocytes obtained from HHR and NHR hearts at age 20 to 30 weeks was evaluated, a prefailure time point selected as a disease progression stage before emergence of premature mortality in HHR. This was considered a time point at which the most consistent phenotypic information could be obtained about the status of electromechanical coupling priming the HHR for failure, and when cardiomyocyte isolation yield could be most reproducible.

HFpEF in the HHR was associated with significant cardiomyocyte enlargement (Figure 3A and 3B, Table S2) determined microscopically from single myocyte dimensions and electrophysiologically by membrane capacitance. Radial and longitudinal cell dimensions were increased similarly (>20%). Thus, hypertrophy at organ and cellular levels was established in the HHR. Functional analysis of shortening performance in isotonically contracting isolated intact cardiomyocytes revealed a dramatic HHR "hypercontractile" state, with almost doubled maximum shortening and shortening kinetic measures allowing overall maintenance of cell activation cycle timing (Figures 3C, 3E, and 4A through 4C). Interestingly, this in vitro hypercontractility was consistent with in vivo hemodynamic measurements obtained using cardiac catheterization (on 50-week animals only), where the maximal rate of pressure development in the HHR was increased (Table S1). HHR myocyte responses to in vitro inotropic intervention (elevated Ca^{2+}, β-stimulation) were modestly potentiated (Figure 4E through 4H).

HHR myocyte diastolic Ca^{2+} levels were elevated and transient amplitude values increased (Figure 3D, 3F, and 3G). Positive correlations between HHR myocyte size and Ca^{2+} levels (but not shortening responses) were detected (Figure 3H through 3J), suggesting a hypertrophy-dependent phenomenon of Ca^{2+} load augmentation. For individual activation cycles, myocyte-shortening Ca^{2+} "phase-loop" plots were constructed. During the relaxation phase, the descending portion of the loop provides a dynamic index of myofilament Ca^{2+} sensitivity. A right shift in HHR myocyte loop relaxation phase provided evidence of decreased myofilament Ca^{2+} responsiveness in the hypertrophic myocytes,

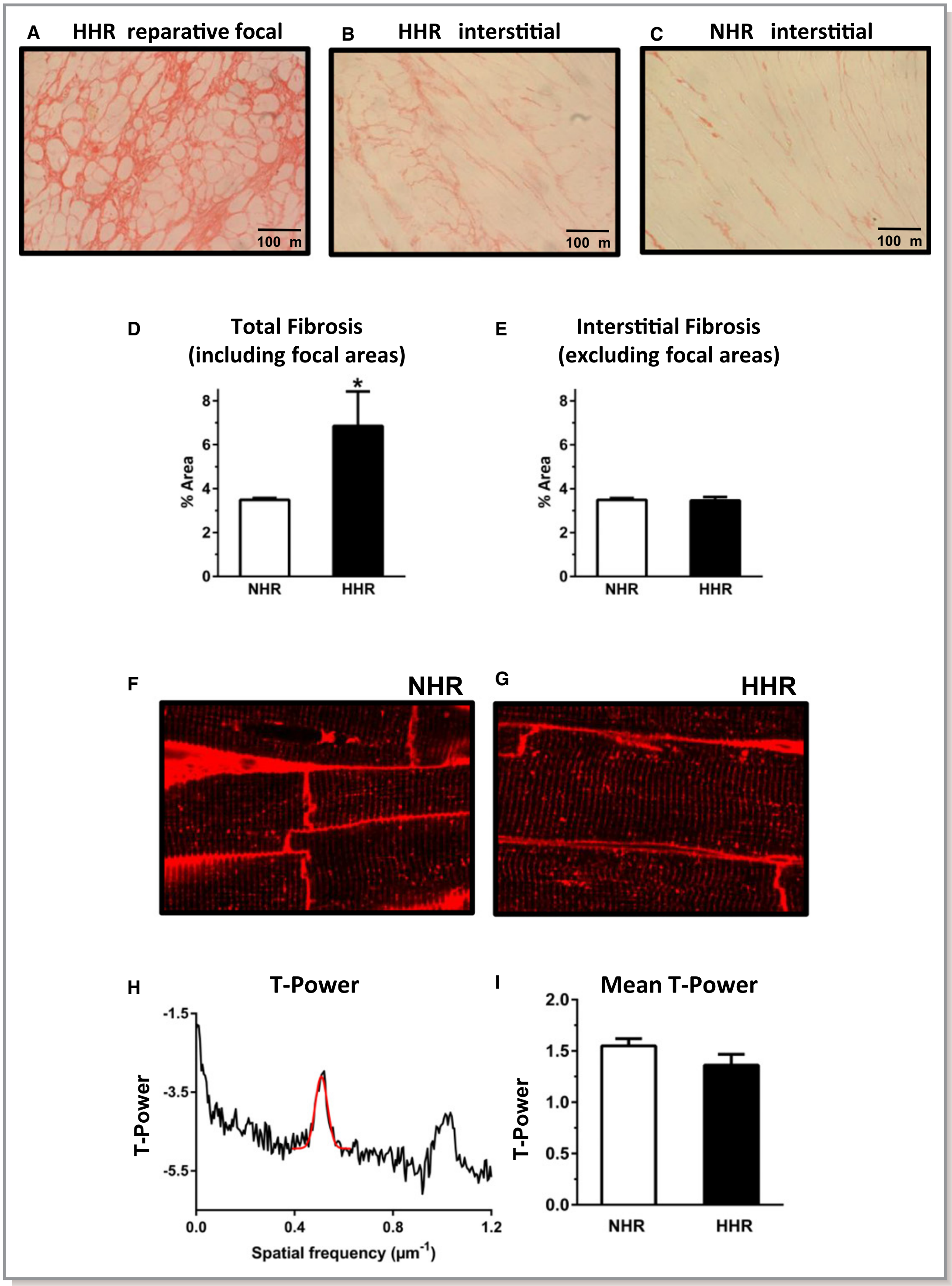

Figure 2. Extracellular matrix disrupted by fibrotic foci with progressing HFpEF, yet maintained cardiomyocyte ultrastructural integrity (50 weeks). A through C, Picrosirius red collagen histology. Fibrotic foci hypertrophic heart rat (HHR), interstitial fibrosis normal heart rat (NHR) and HHR. D and E, Fibrosis densitometry: total and interstitial excluding focal areas in HHR. F and G, T-tubule labeling with wheat germ agglutinin Alex-594 shows t-system geometry regularity in sectioned myocardium of HHR and NHR. H and I, Depiction of T-tubule power vs spatial frequency in longitudinal dimension for HHR and NHR evidenced high level of T-tubule structural integrity in HHR and NHR. Graphs show mean ± SEM. For D and E, Student *t* test, n=20 images/N=5 hearts. For F and G, n=18/group; N=3 hearts/group.

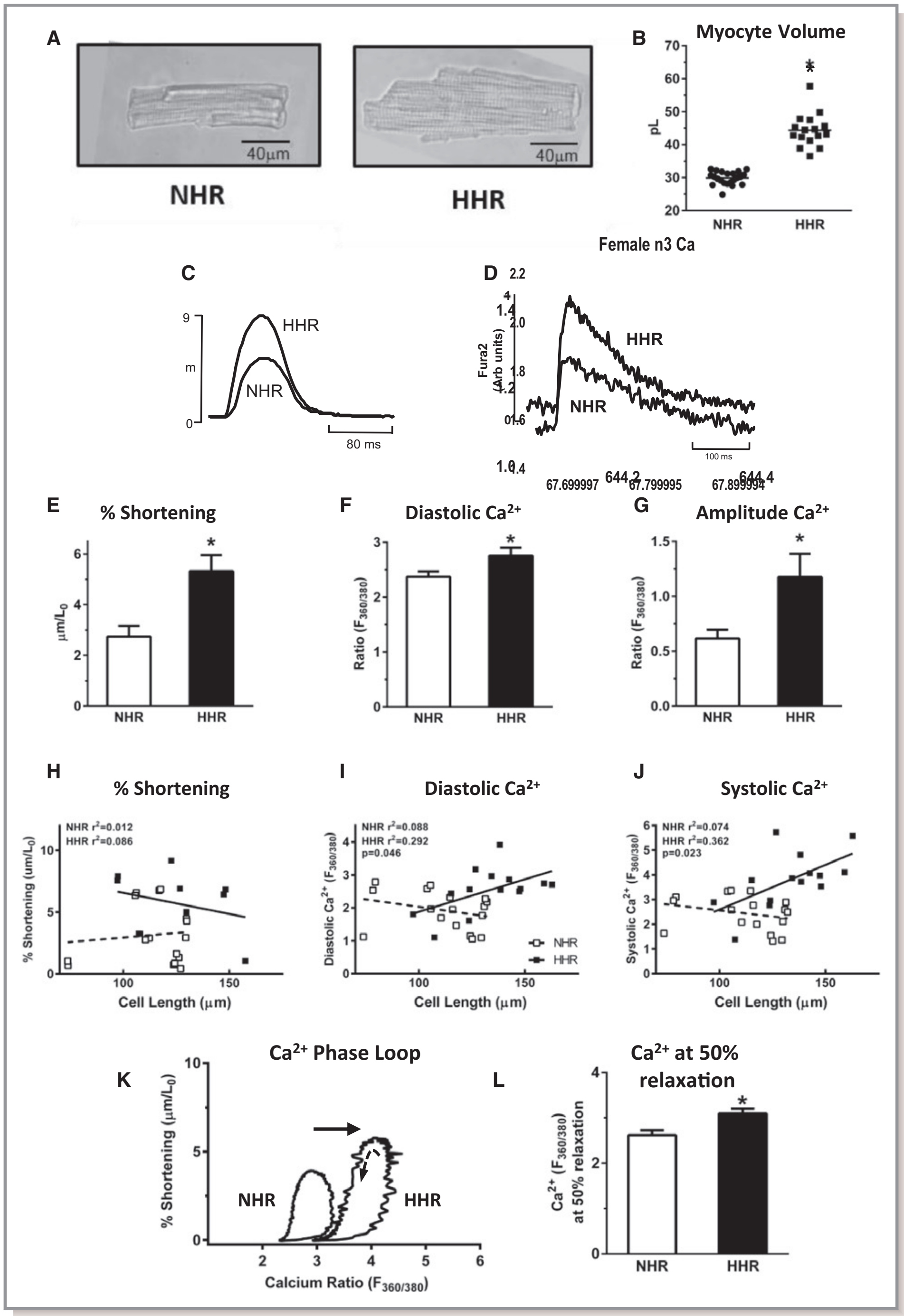

Figure 3. HHR cardiomyocyte hypercontractility characterizes progression to failure with preserved systolic function (20–30 weeks). A, Bright field normal heart rat (NHR) and hypertrophic heart rat (HHR) cardiomyocyte micrographs. B, Mean computed cardiomyocyte volume from 2-dimensional isolated myocyte measurements (n=mean 50 cells for N=16–22 hearts). C and D, Fura-2 loaded isolated myocyte exemplar records: shortening and Ca^{2+} transients. E through G, Cardiomyocyte mean maximum % shortening (normalized for myocyte length), and mean Ca^{2+} diastolic and twitch amplitude levels (n=16–17 cells for N=10 hearts/group). H through J, Regression plots: myocyte size (μm) vs % shortening, diastolic Ca^{2+} and peak systolic Ca^{2+} levels (n=16–17 cells from N=10 hearts/group). K and L, Exemplar "Phase-loop" plots of cardiomyocyte length vs Ca^{2+} during activation cycle show HHR right-shift, with significantly higher Ca^{2+} at 50% myocyte relaxation, indicating reduced sensitivity to Ca^{2+} levels (n=16–17 cells from N=10 hearts/group). Graphs show mean ± SEM, For B, E through G, and L, *$P<0.05$ (Student *t* test). For H through J, *P* value, Pearson's correlation.

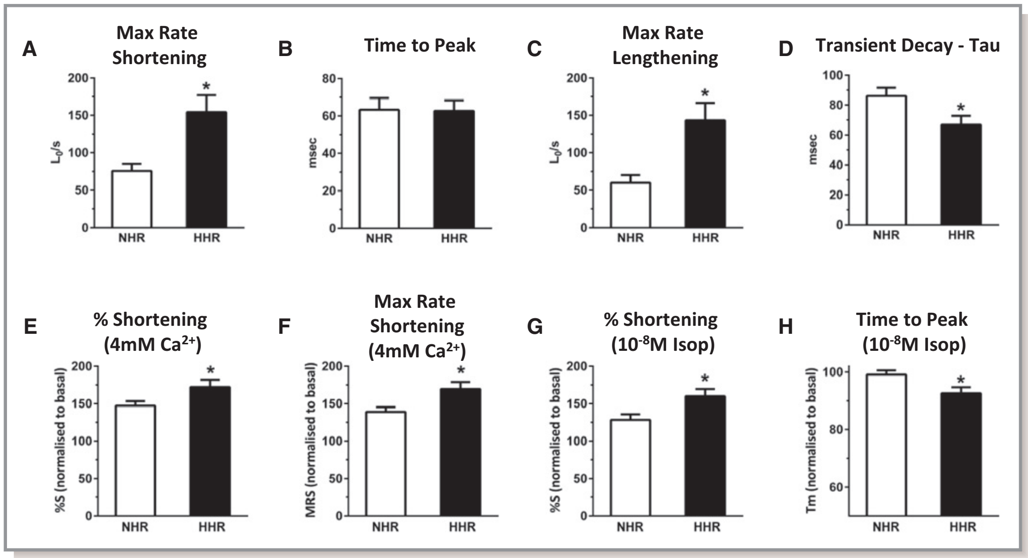

Figure 4. Isolated cardiomyocyte basal shortening parameters and responses to inotropic interventions (20–30 weeks). A through D, Mean maximum rate of shortening, time of peak shortening, maximum rate of lengthening and Ca^{2+} transient decay time constant (τ=1/e). E and F, Mean changes in shortening (%S) and maximum rate of shortening in response to an increase in superfusate [Ca^{2+}] from 1.5 to 4 mmol/L for normal heart rat (NHR) and hypertrophic heart rat (HHR). G and H, Mean changes in shortening (%S) and time to peak shortening in response to isoproterenol treatment (10^{-8} mol/L) for NHR and HHR. Graphs show mean ± SEM. For each myocyte group, reference performance level under control pretreatment conditions designated 100%. ($^{*}P<0.05$, Student *t* test, n=17 to 19 cells from N=4 to 6 hearts/group).

quantified by measurement of Ca^{2+} at 50% myocyte relaxation (Figure 3K and 3L).

No differences in HHR and NHR isoform type and total phosphorylation status of titin (an extensible protein with a role in determining sarcomeric stiffness) were identified (Figure S5, Table S3).

Elevated Myocyte Ca^{2+} Loading in Diastolic Dysfunction Linked With Increased I-Ca^{2+} Current Density

I-Ca measured using whole-cell patch clamp methodology, were significantly elevated in prefailure HHR myocytes relative to NHR (holding potential −90 mV), with peak I-Ca density (normalized for cell size) increased by ≈65% in HHRs (Figure 5A through 5C). Current measured from −90 mV substantially comprises the L-type Ca^{2+} current. Consistent current density differences were also observed for current ensembles measured from holding potentials −50 and −115 mV. There was no evidence of HHR-specific low-voltage activated currents (absence of inflexion in current plots from −115 and −90 mV holding potentials) (Figure S6). Capacity for Ca^{2+} flux via the Na^{+}/Ca^{2+} exchanger was examined electrophysiologically, as this transporter upregulation is implicated in arrhythmogenicity.[21] In forward mode operation (ie, Ca^{2+} extrusion, inward current, from −90 mV) and reverse mode operation (to +40 mV), the I-NCX densities (pA/pF) were not different for NHR and HHR (Figure 5D through 5F). Protein expression data indicate that NCX1 levels are also not different in the NHR and HHR (Figure S7).

HHR In Vivo and In Vitro Dysrhythmic Substrates—Cardiomyocyte Ca^{2+} Handling Instability

In vivo occurrence of prominent arrhythmic episodes in HHR at 20 to 30 weeks and beyond was confirmed by external lead ECG—events not observed in NHR (Figure 6A). Significant prolongation of mean HHR QRS interval was quantified, consistent with ventricular abnormality (Figure S8). Electromechanical instability in isolated HHR cardiomyocytes was also quantifiable, with a 2-fold increase in occurrence of spontaneous SR Ca^{2+} release events (Figure 6B) indicative of SR Ca^{2+} store overload susceptibility. Regulation of activator Ca^{2+} and SR Ca^{2+} load stability is crucially dependent on expression and activation levels of key proteins involved in SR Ca^{2+} uptake and release. In the HHR, total expression levels of the SR Ca^{2+} ATPase (SERCA2a), phospholamban (the SERCA2a negative regulator), and the SR Ca^{2+} release channel protein were significantly reduced. In contrast, the phosphorylation states of these proteins were markedly increased—effects that act to relieve SR pump inhibition and promote SR Ca^{2+} release channel trigger sensitivity and leak (Figure 6C and 6D). Expression-level reduction and increased activation status of the upstream regulator Ca^{2+}-

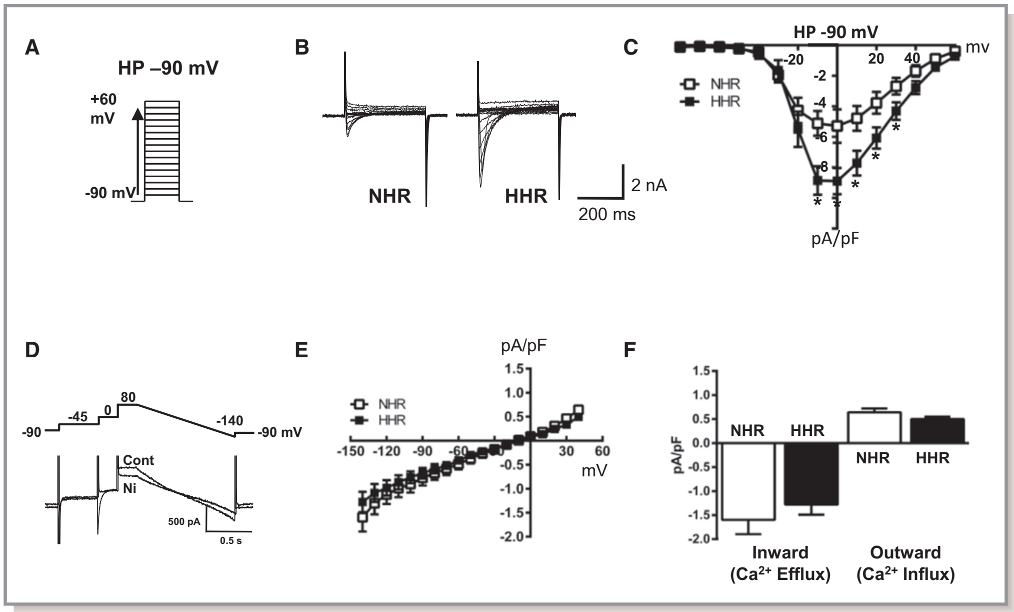

Figure 5. Elevated myocyte Ca^{2+} loading in diastolic dysfunction linked with increased I-Ca current density (20–30 weeks). A, I-Ca voltage clamp protocol, holding potential −90 mV. B, Representative I-Ca current traces. C, Mean I-Ca current densities (pA/pF). D, Na^{+}/Ca^{2+} exchange current (I-NCX) voltage clamp protocol and representative current traces, I-NCX quantification by current subtraction ±5 mmol/L $NiCl_2$. E, Mean normalized I-NCX determined at ramp test potentials −140 to +40 mV. F, Mean maximum inward I-NCX density (inward and outward mode operation). Graphs show mean ± SEM (*$P<0.05$, 1 way ANOVA with repeated measures, n=27–30 cells for N=9 hearts/group).

calmodulin dependent kinase II (CaMKII) was observed (Figure 6E), consistent with increased activation of the SR Ca^{2+} effector CaMKII target proteins. Evidence indicates that SERCA2 activity is increased on the basis of hyperphosphorylation of the SR pump regulator phospholamban (Figure 6C) and more rapid rate of transient decay in the HHR (Figure 4D). Pilot caffeine spritz experiments also indicate SR Ca load is elevated in the HHR (Figure S9).

Discussion

In this study, we present and characterize a new experimental model of HFpEF—and identify a cardiomyocyte pathology that contrasts conspicuously with that generally reported in HFrEF conditions. In vivo, the HHR displays marked diastolic dysfunction in the context of relatively preserved systolic function. The in vitro cardiomyocyte functional studies of Ca^{2+} handling and shortening performance surprisingly reveal a hypercontractile state underlying the in vivo diastolic dysfunction. Other notable features include those of focal and relatively discrete areas of interstitial fibrosis and the in vivo predisposition to dysrhythmia and sudden death. The cardiomyocyte phenotypes of higher incidence of spontaneous Ca^{2+} transients and molecular changes consistent with SR Ca^{2+} instability provide evidence of cellular arrhythmogenic substrate. Thus, preservation of EF is apparently achieved through hypercontractility, which compensates for cardiomyocyte deficit and structural slippage at fibrotic foci. These findings represent a potentially important advance in understanding the cellular etiology of HFpEF. We demonstrate that the cardiomyocyte Ca^{2+} handling and contractile abnormalities in HFpEF are fundamentally different to the cellular electromechanical features usually observed in association with HFrEF.

The HHR provides a model that closely reflects clinical HFpEF. We have previously identified early emergence of cardiac hypertrophy in adult HHR, linked with deficient cardiomyocyte endowment in the neonatal heart.[16,17] Now in this longitudinal study, we demonstrate that hypertrophic progression to failure occurs with animal aging and without additional intervention. At failure, diastolic dysfunction is marked, while ejection fraction and fractional shortening are largely maintained, with normal end-diastolic volume index. We show that premature mortality in the HHR is associated with evidence of ventricular stiffness as indexed by elevated end-diastolic pressure-volume relationship (EDPVR) and impaired filling, focal reparative (interstitial) fibrosis, and prominent cardiomyocyte hypertrophy. Elevated brain natriuretic peptide has been shown previously.[17] Together, these findings indicate the HHRs die prematurely from both fatal cardiac arrhythmias and chronic diastolic heart failure. This constellation of phenotypes is consistent with generally

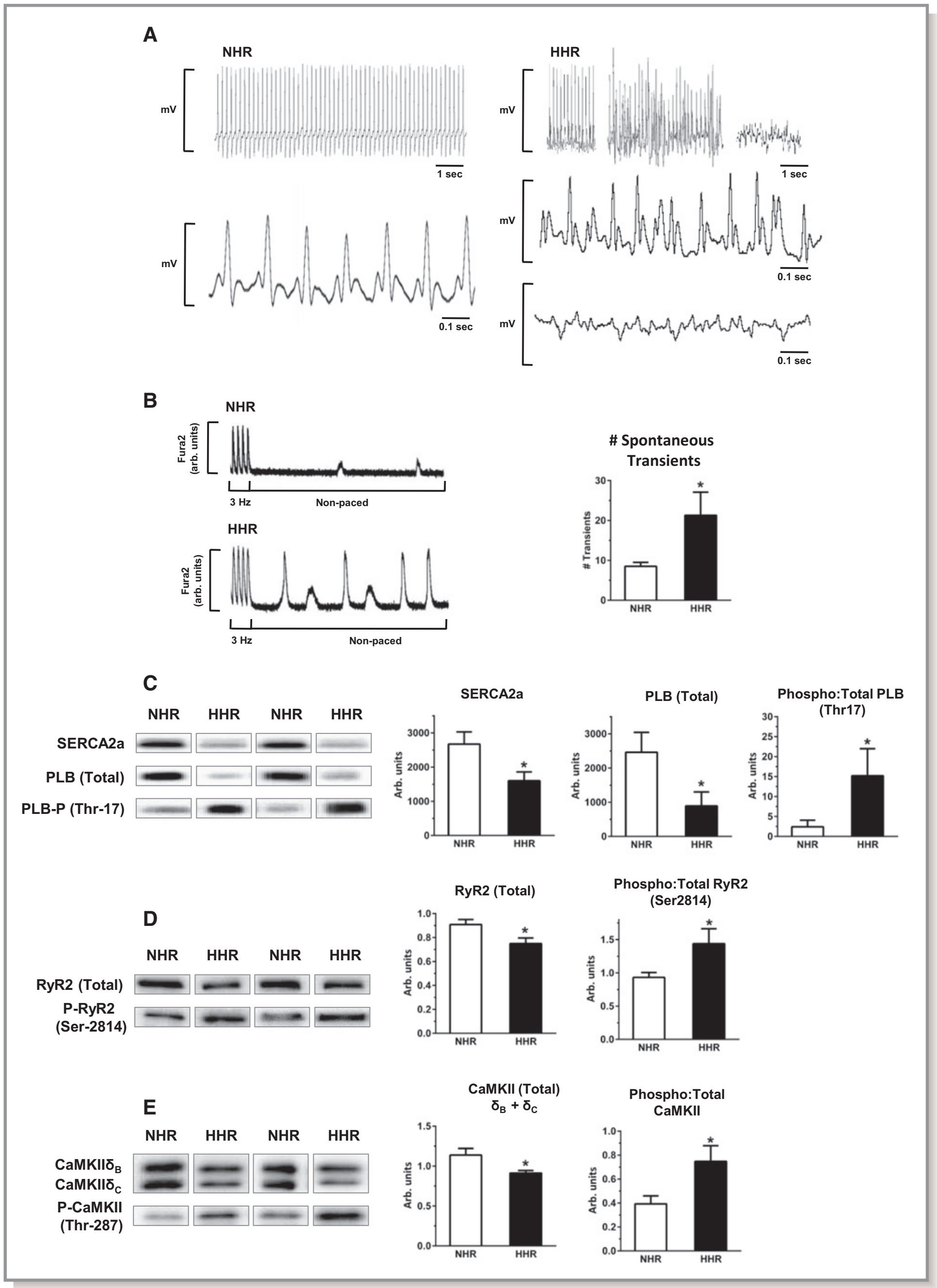

Figure 6. HHR in vivo and in vitro dysrhythmic substrates—cardiomyocyte Ca handling instability. A, Exemplar ECG records depicting stable sinus rhythm in normal heart rat (NHR) vs episodic hypertrophic heart rat (HHR) dysrhythmic periods. B, Spontaneous Ca^{2+} release events in nonpaced cardiomyocytes, quantified over 30 seconds. ($^*P<0.05$, Student *t* test, n=21–23 cells/group). C through E, Immunoblot analyses of total protein expression and phosphorylation levels, left ventricular tissue homogenate, for SERCA2a, PLB (Ser-17), RYR2 (Ser2814), CaMKII (combined δB & δC isoform, Thr287) ($^*P<0.05$, Student *t* test, N=10 hearts/group). Graphs show mean ± SEM. For A, age 30 to 50 weeks. For B through E, age 20 to 30 weeks.

accepted clinical benchmarks for HFpEF diagnosis—notwithstanding the inherent syndrome heterogeneity.[7–9]

HHR cardiomyocytes exhibit hypercontractile status and high Ca^{2+} operational levels linked with arrhythmogenic vulnerability. These cardiomyocyte operational characteristics contrast dramatically with the canonical view of the hypertrophied and failing cardiomyocyte—a phenotype of HFrEF defined primarily in the setting of hemodynamic loading and typified by impaired contractility and reduced activator Ca^{2+} availability.[11] Systolic function preservation in the HHR likely derives from the large increase in density of the L-type Ca^{2+} channel, underpinning cardiomyocyte hypercontractility. The developmental mechano-transduction link between increased myocyte dimension and hyperperformance is unknown but appears to be a characteristic specific for pathologic myocyte enlargement as expressed in the HHR. In HHRs there was a significant and positive correlation of cell dimension with systolic and with diastolic Ca^{2+} levels (ie, larger myocytes exhibited more elevation in Ca^{2+} operational levels). This relationship was absent in the NHR. This finding supports the speculation that a signaling process may operate to link hypertrophy induction and shift of Ca^{2+} operational levels in the evolving HFpEF context. Temporally and spatially averaged elevations in cardiomyocyte Ca^{2+} levels have been linked with induction of experimental hypertrophy.[22] Elevated Ca^{2+} levels have been observed in ventricular biopsy specimens of patients diagnosed with hypertensive heart disease exhibiting HFpEF symptoms (in the absence of any disturbance of Na^+ perturbation).[23] Further work is required to evaluate the myocyte hypertrophy-Ca^{2+} relationship and potential interventional opportunities specifically in the HFpEF setting. In the HHR, we also found an indirect indication of myofilament Ca^{2+} desensitization—this may suggest a protective adaptation in response to the high Ca^{2+} cycling environment. In the HHR, it will be etiologically informative to confirm that the elevated Ca^{2+} transient phenotype persists to point of failure, and further longitudinal studies are required.

It may be hypothesized that the cardiomyocyte deficit in HHR mediates compensatory hypertrophy of surviving myocytes through mechano-transduced shifts in molecular management of Ca^{2+} influx. Increased voltage-activated Ca^{2+} current was linked with both increased Ca^{2+} transient amplitude and peak myocyte shortening. Our data do not allow quantitative dissection of the Ca^{2+} channel/SERCA2 contributions to the transient but do support the proposition that the increased L-type Ca^{2+} channel current provides the primary driver for elevated Ca^{2+} transient, and a consequentially activated SERCA2 allows for enhanced SR Ca^{2+} releasable load. Further experimental work with cardiomyocytes using pharmacologic agents is required to resolve these questions, including longitudinal studies that examine the early emergence of the Ca^{2+} channel phenotype.

Notably, no functional difference in Na^+/Ca^{2+} current density was detected between HHR and NHR cardiomyocytes. This contrasts with previous experimental demonstration of Na^+/Ca^{2+} exchanger upregulation as a key process in transition to failure in HFrEF.[21] These findings also differ from observations made in a setting of diastolic dysfunction where the primary insult is acute renal intervention (nephrectomy) and cardiomyocyte systolic Ca^{2+} levels and contractility are unchanged.[24] Protein expression data indicate that NCX1 levels are also not different in the two strains. Thus, an explanation of increased activation of the NCX in HHR seems likely, to ensure balance between Ca^{2+} influx/efflux. NCX activity is known to be allosterically regulated by intracellular Ca^{2+}. There is also evidence of regulation of exchanger activity by protein posttranslation modification—either directly or by accessory protein (eg, phospholemman) modification. A comprehensive understanding of the manner in which posttranslational modifications regulate NCX has yet to be resolved.

The notion that early development myocardial stress events independent of systemic load may be involved in hypertrophy initiation is consistent with evidence that diastolic dysfunction in the spontaneously hypertensive rat is detectable before onset of hypertrophy and hypertension.[25] Our finding that diastolic dysfunction is apparent in very young animals is also indicative of early compliance abnormality contributing to abnormal myocardial mechanical and structural modeling.

Diastolic dysfunction can arise from altered internal cardiomyocyte conditions including high interbeat diastolic Ca^{2+} levels that limit relaxation and/or increase sarcomere structural stiffness.[9,26] In the HHR, the elevated resting Ca^{2+} levels likely contribute to diastolic dysfunction, and the data suggest that this may be attributed to increased SR Ca^{2+} "leakiness" mediated via CaMKII activation-induced ryanodine receptor sensitization through hyperphosphorylation. Direct CaMKII hyperphosphorylation of titin has also been associated with sarcomere stiffness.[27] In this study, it was not possible to detect a net change in total titin phosphorylation state, suggesting that any CaMKII phosphorylation actions are offset by other kinase signaling events. Titin isoform expression was not different in HHR—consistent with observations in other rodent models of diastolic dysfunction.[27]

Arrhythmogenic vulnerability in various settings has been associated with ectopic diastolic events of spontaneous SR Ca^{2+} release. In the HHR the preserved SR "reloading" capacity (through phospho-phospholamban-mediated SERCa2 disinhibition), in association with ryanodine receptor 2 sensitization (a combination of ryanodine receptor 2 hyperphosphorylation and SR load elevation), provides a substrate for spontaneous SR Ca^{2+} release activity. Our findings show that neither altered Na^+/Ca^{2+} exchanger functional capacity or disrupted T-tubule geometry are preconditions for occurrence of SR spontaneous Ca^{2+} release triggered arrhythmogenic events—that high Ca^{2+} operational levels independently confer instability. Data from in vitro (intact cardiomyocytes) and in vivo (ECG) experiments produced direct evidence of HHR arrhythmogenic propensity, consistent with sudden cardiac death–related HHR mortality during failure progression. This arrhythmogenic vulnerability evaluated in vitro may be even more accentuated in vivo given that the HHR neurohumoral milieu involves factors that differentially elevate heart rate and may predispose to arrhythmia. In considering the demonstrated in vitro differences in HHR and NHR cardiomyocyte performance, it is important to appreciate that the in vivo disparity in heart rate is an additional major consideration.

Myocardial fibrosis/extracellular matrix remodeling also plays a role in diastolic dysfunction.[13] In the HHR, regions of focal fibrosis were evident, particularly prominent near the interventricular septum, which were not present in the NHR. Our histologic findings in HHR ventricular tissue might reflect regional vulnerability to localized perimysial layer shear and rupture[28] more extensive in the septum confluence, producing areas of reparative fibrosis associated with, and possibly contributing to, the development of global ventricular stiffness. Involvement of cardiomyocyte-specific inflammatory response may also be involved—we have recently demonstrated activation of lipocalin-2 mediated inflammatory pathways in the HHR.[29] A role for cardiomyocyte hypercontractility in predisposing for mechanical shear damage is feasible. Indeed, fibrosis and slippage might change the mechanics of the cardiac syncytium such that myocyte hypercontractility is not translated to increased systolic function in vivo. In overview, the etiologic processes that culminate in HHR HFpEF likely have a long-term latent origin. We have previously reported that hypertrophy in the HHR is linked with reduced cardiomyocyte population at an early growth stage.[16,17] This myocyte deficit apparently mediates compensatory hypertrophy and hypercontractility of diminished myocyte endowment via a mechano-transduction response (yet to be characterized). Hypercontractility is associated with regions of tissue mechanical vulnerability—myocyte rupture and fibrotic replacement. Thus, with progression toward failure, even while the surviving cardiomyocyte population may be hypercontractile, the remodeled tissue geometry and accumulating focal fibrosis undermines integrity. Overall, ejection fraction is relatively conserved while function (primarily diastolic) is compromised. Clinically, a range of earlier life cardiac stresses and genetic factors could be expected to contribute to HFpEF predisposition and ultimate disease emergence.

In summary, here we report the characterization of a new model of HFpEF and provide the first demonstration of cardiomyocyte cellular pathophysiology underlying this increasingly prevalent form of heart failure. Therapies that have been largely successful in treatment of HFrEF have been targeted at suppressing neurohumoral signaling axes involving the renin-angiotensin-aldosterone system and β-adrenoceptors.[3,14] Recently, evaluation of phosphodiesterase-5 inhibition also reported lack of clinical improvement in HFpEF.[30] While these therapies may reduce morbidity in some HFpEF cohorts, mortality reduction has not be achieved in trials to date.[31] Now this investigation provides important mechanistic insight into the contrasting cellular etiologies of HFpEF and HFrEF, and represents a conceptual advance to be exploited for targeted development of HFpEF-specific therapeutic intervention. Based on this study's novel findings, further studies of the signaling pathways involved and the effects of systemic secondary insults in shaping HFpEF failure development may now be pursued. As a new preclinical platform, the HHR provides a model for building multisystem pathology states through additional interventions that capture the spectrum of HFpEF phenotypes and comorbidities observed clinically. With this new understanding of the cardiopathology mechanism, there is potential opportunity for preclinical innovation in responding to the HFpEF challenge.

Sources of Funding

Career Fellowship support provided through the National Heart Foundation of Australia (Bell, Porrello), the National Health and Medical Research Council (NHMRC) of Australia (Porrello) and the University of Melbourne R. Douglas Wright Faculty Trust (Bell), Research support provided through NHMRC (Delbridge, Harrap, Bell, Erickson, Kalman).

Disclosures

None.

References

1. Greenberg B. Heart failure preserved ejection fraction with coronary artery disease: time for a new classification? *J Am Coll Cardiol*. 2014;63:2828–2830.
2. Borlaug BA. The pathophysiology of heart failure with preserved ejection fraction. *Nat Rev Cardiol*. 2014;11:507–515.
3. Roh J, Houstis N, Rosenzweig A. Why don't we have proven treatments for HFpEF? *Circ Res*. 2017;120:1243–1245.
4. Senni M, Paulus WJ, Gavazzi A, Fraser AG, Diez J, Solomon SD, Smiseth OA, Guazzi M, Lam CS, Maggioni AP, Tschope C, Metra M, Hummel SL, Edelmann F, Ambrosio G, Stewart Coats AJ, Filippatos GS, Gheorghiade M, Anker SD, Levy D, Pfeffer MA, Stough WG, Pieske BM. New strategies for heart failure with preserved ejection fraction: the importance of targeted therapies for heart failure phenotypes. *Eur Heart J*. 2014;35:2797–2815.
5. de Simone G, Gottdiener JS, Chinali M, Maurer MS. Left ventricular mass predicts heart failure not related to previous myocardial infarction: the Cardiovascular Health Study. *Eur Heart J*. 2008;29:741–747.
6. Shah SJ, Kitzman DW, Borlaug BA, van Heerebeek L, Zile MR, Kass DA, Paulus WJ. Phenotype-specific treatment of heart failure with preserved ejection fraction: a multiorgan roadmap. *Circulation*. 2016;134:73–90.
7. Shah SJ, Katz DH, Selveraj S, Burke MA, Yancy CW, Gheorghiade M, Bonow RO, Huang CC, Deo RC. Phenomapping for novel classification of heart failure with preserved ejection fraction. *Circulation*. 2015;131:269–279.
8. Kelly JP, Mentz RJ, Mebazaa A, Voors AA, Butler J, Roessig L, Fiuzat M, Zannad F, Pitt B, O'Connor CM, Lam CS. Patient selection in heart failure with preserved ejection fraction clinical trials. *J Am Coll Cardiol*. 2015;65:1668–1682.
9. Paulus WJ, Tschope C. A novel paradigm for heart failure with preserved ejection fraction: comorbidities drive myocardial dysfunction and remodeling through coronary microvascular endothelial inflammation. *J Am Coll Cardiol*. 2013;62:263–271.
10. Ponikowski P; Task Force Members. 2016 ESC guidelines for the diagnosis and treatment of acute and chronic heart failure. *Eur Heart J*. 2016;37:2129–2200.
11. Luo M, Anderson ME. Mechanisms of altered Ca^{2+} handling in heart failure. *Circ Res*. 2013;113:690–708.

12. Houser SR, Margulies KB, Murphy AM, Spinale FG, Francis GS, Prabhu SD, Rockman HA, Kass DA, Molkentin JD, Sussman MA, Koch WJ; American Heart Association Council on Basic Cardiovascular Sciences CoCC, Council on Functional Genomics and Translational Biology. Animal models of heart failure: a scientific statement from the American Heart Association. *Circ Res*. 2012;111:131–150.
13. Braunwald E. The war against heart failure: the Lancet lecture. *Lancet*. 2014;385:812–824.
14. Desai AS, Jhund PS. After TOPCAT: what to do now in heart failure with preserved ejection fraction. *Eur Heart J*. 2016;37:3135–3140.
15. Conceição G, Heinonen I, Lourenço AP, Duncker DJ, Falcão-Pires I. Animal models of heart failure with preserved ejection fraction. *Neth Heart J*. 2016;24:275–286.
16. Harrap SB, Danes VR, Ellis JA, Griffiths CD, Jones EF, Delbridge LM. The hypertrophic heart rat: a new normotensive model of genetic cardiac and cardiomyocyte hypertrophy. *Physiol Genomics*. 2002;9:43–48.
17. Porrello ER, Bell JR, Schertzer JD, Curl CL, McMullen JR, Mellor KM, Ritchie RH, Lynch GS, Harrap SB, Thomas WG, Delbridge LM. Heritable pathologic cardiac hypertrophy in adulthood is preceded by neonatal cardiac growth restriction. *Am J Physiol Regul Integr Comp Physiol*. 2009;296:R672–R680.
18. Innes BA, McLauglin MG, Kapuscinski MK, Jacob HJ, Harrap SB. Independent genetic susceptibility to cardiac hypertrophy in inherited hypertension. *Hypertension*. 1998;31:741–746.
19. Mellor KM, Bell JR, Young MJ, Ritchie RH, Delbridge LM. Myocardial autophagy activation and suppressed survival signaling is associated with insulin resistance in fructose-fed mice. *J Mol Cell Cardiol*. 2011;50:1035–1043.
20. Domenighetti AA, Danes VR, Curl CL, Favaloro JM, Proietto J, Delbridge LM. Targeted GLUT-4 deficiency in the heart induces cardiomyocyte hypertrophy and impaired contractility linked with Ca^{2+} and proton flux dysregulation. *J Mol Cell Cardiol*. 2010;48:663–672.
21. Rodriguez JS, Velez Rueda JO, Salas M, Becerra R, Di Carlo MN, Said M, Vittone L, Rinaldi G, Portiansky EL, Mundiña-Weilenmann C, Palomeque J, Mattiazzi A. Increased Na^{+}/Ca^{2+} exchanger expression/activity constitutes a point of inflection in the progression to heart failure of hypertensive rats. *PLoS One*. 2014;9:e96400. doi: 10.1371/journal.pone.0096400.
22. Wu X, Zhang T, Bossuyt J, Li X, McKinsey TA, Dedman JR, Olson EN, Chen J, Brown JH, Bers DM. Local InsP3-dependent perinuclear Ca^{2+} signaling in cardiac myocyte excitation-transcription coupling. *J Clin Invest*. 2006;116:675–682.
23. Runte KE, Bell SP, Selby DE, Häußler TN, Ashikaga T, LeWinter MM, Palmer BM, Meyer M. Relaxation and the role of calcium in isolated contracting myocardium from patients with hypertensive heart disease and heart failure with preserved ejection fraction. *Circ Heart Fail*. 2017;10: e004311.
24. Primessnig U, Schönleitner P, Höll A, Pfeiffer S, Bracic T, Rau T, Kapl M, Stojakovic T, Glasnov T, Leineweber K, Wakula P, Antoons G, Pieske B, Heinzel FR. Novel pathomechanisms of cardiomyocyte dysfunction in a model of heart failure with preserved ejection fraction. *Eur J Heart Fail*. 2016;18:987–997.
25. Dupont S, Maizel J, Mentaverri R, Chillon JM, Six I, Giummelly P, Brazier M, Choukroun G, Tribouilloy C, Massy ZA, Slama M. The onset of left ventricular diastolic dysfunction in SHR rats is not related to hypertrophy or hypertension. *Am J Physiol Heart Circ Physiol*. 2012;302:H1524–H1532.
26. van Heerebeek L, Borbely A, Niessen HW, Bronzwaer JG, van der Velden J, Stienen GJ, Linke WA, Laarman GJ, Paulus WJ. Myocardial structure and function differ in systolic and diastolic heart failure. *Circulation*. 2006;113:1966–1973.
27. Hamdani N, Krysiak J, Kreusser MM, Neef S, Dos Remedios CG, Maier LS, Krüger M, Backs J, Linke WA. Crucial role for Ca2(+)/calmodulin-dependent protein kinase-II in regulating diastolic stress of normal and failing hearts via titin phosphorylation. *Circ Res*. 2013;112:664–674.
28. Pope AJ, Sands GB, Smaill BH, LeGrice IJ. Three-dimensional transmural organization of perimysial collagen in the heart. *Am J Physiol*. 2008;295: H1243–H1252.
29. Marques FZ, Prestes PR, Byars SG, Ritchie SC, Würtz P, Patel SK, Booth SA, Rana I, Minoda Y, Berzins SP, Curl CL, Bell JR, Wai B, Srivastava PM, Kangas AJ, Soininen P, Ruohonen S, Kähönen M, Lehtimäki T, Raitoharju E, Havulinna A, Perola M, Raitakari O, Salomaa V, Ala-Korpela M, Kettunen J, McGlynn M, Kelly J, Wlodek ME, Lewandowski PA, Delbridge LM, Burrell LM, Inouye M, Harrap SB, Charchar FJ. Experimental and human evidence for lipocalin-2 (neutrophil gelatinase-associated lipocalin [NGAL]) in the development of cardiac hypertrophy and heart failure. *J Am Heart Assoc*. 2017;6:e005971. doi: 10.1161/JAHA.117.005971.
30. Redfield MM, Chen HH, Borlaug BA, Semigran MJ, Lee KL, Lewis G, LeWinter MM, Rouleau JL, Bull DA, Mann DL, Deswal A, Stevenson LW, Givertz MM, Ofili EO, O'Connor CM, Felker GM, Goldsmith SR, Bart BA, McNulty SE, Ibarra JC, Lin G, Oh JK, Patel MR, Kim RJ, Tracy RP, Velazquez EJ, Anstrom KJ, Hernandez AF, Mascette AM, Braunwald E; RELAX Trial. Effect of phosphodiesterase-5 inhibition on exercise capacity and clinical status in heart failure with preserved ejection fraction: a randomized clinical trial. *JAMA*. 2013;309:1268–1277.
31. Kosmala W, Rojek A, Przewlocka-Kosmala M, Wright L, Mysiak A, Marwick TH. Effect of aldosterone antagonism on exercise tolerance in heart failure with preserved ejection fraction. *J Am Coll Cardiol*. 2016;68:1823–1834.

SUPPLEMENTAL MATERIAL

Data S1.

Supplemental Methods

On request to the Corresponding author, the data, analytic methods, and study materials will be/have been made available to other researchers for purposes of reproducing the results or replicating the procedure**.**

Development and maintenance of the Hypertrophic Heart Rat (HHR) and control Normal Heart Rat (NHR) strains

A novel normotensive, hypertrophic rat strain has been generated through selection and cross breeding of Fischer 344 and Spontaneously Hypertensive Rat (SHR) strain progenitors.[1] We had demonstrated previously that the SHR possessed genetic determinants of cardiac hypertrophy, independent of blood pressure.[2] For the first 4 generations males and females were selected for the HHR line which exhibited elevated left ventricular echo dimensions relative to the corresponding mating pairs in the NHR line. Both lines were stabilized through 21 generations of in-breeding to achieve strain status.[3] The control Normal Heart Rat (NHR) was co-derived from the same original F2 population. Thus, the Hypertrophic Heart Rat (HHR) and Normal Heart Rat (NHR) strains constitute genetically stabilized models for investigation of non-load induced hypertrophy, with natural disease history. HHR and NHR genomic analysis has identified variants unique to each strain, including single nucleotide polymorphisms, insertions & deletions, and copy number variations. [3] Experiments were performed using male HHR and NHR at ages indicated. This study was confined to single sex evaluation and pooling of sex data avoided as previous studies have identified sex differences which will be further explored in additional studies. All animals were housed under a 12-hour light/dark cycle with water and standard chow provided *ad libitum.*

Echocardiography

Cardiac structure and function were evaluated by transthoracic 2-dimensional B- and M-mode echocardiography (GE Vivid 9; 15mHz i13L linear array transducer) performed under light anesthesia (inhalation of isoflurane at 1.5%) ensuring temperature maintenance of animals. Acquisition and offline analysis was performed with GE EchoPac software. The parasternal short axis was utilized for *systolic parameters* (interventricular septum IVS, left ventricular posterior wall LVPW, left ventricular dimension LVID, fractional shortening FS, ejection fraction EF, heart rate HR), and mitral valve blood flow and tissue Doppler were measured in apical four chamber view for *diastolic parameters* (E/A, isovolumic relaxation time IVRT, mitral valve deceleration time MVDecT, E'/A', E'/E). Normalized parameters for wall dimension indices were calculated for HHR by scaling measured values by the ratio of animal body weight relative to NHR mean. For each measurement at least three consecutive cycles were sampled.

Electrocardiograms

Electrocardiograms (ECG) were obtained under light anesthesia (inhalation of isoflurane at 1.5%) using external clip leads in standard configuration. The ECG signal was amplified (ADInstruments Animal Bio Amp), digitally acquired, filtered, displayed and analyzed using a MacLab data acquisition system.

Hemodynamic measurements

24-h blood pressure profiles in freely moving conscious rats were monitored over a continuous period of 7 days by telemetry. Two weeks prior to recording, rats were implanted with blood pressure telemeters (model TA11PA-C40, Data Sciences International) in the abdominal aorta according to the method detailed by the supplier. Systolic and diastolic blood pressure, and mean arterial pressure were recorded as the reduced mean of a 10-s sampling interval every 10 min using data acquisition and analysis software (Data Sciences International, USA). As previously described[4], to obtain hemodynamic measures by cardiac catheterization animals were anaesthetized with sodium pentobarbital (60mg/kg) and were intubated and ventilated using positive pressure with a tidal volume of 8 to 10% body weight at 70 breaths/min using room air. A 2F miniaturized combined conductance catheter-micromanometer (Model

SPR-838 Millar instruments, Houston, TX) was inserted into the right carotid artery to obtain aortic blood pressure, and then advanced into the left ventricle until stable pressure-volume (PV) loops were obtained. Data were acquired under steady state conditions and during preload reduction. Using the pressure conductance data a range of functional parameters was then calculated (Lab Chart analysis software). These included end diastolic pressure (EDP), maximum rate of pressure change in the ventricle (+dP/dt max), minimum rate of pressure change in the ventricle (-dP/dt min) and the slope of the end diastolic pressure volume relationship (EDPVR).

Histological Analysis of Myocardial Collagen Content

Hearts were fixed in 10% formalin for histological analysis using picrosirius red as previously described.[5] Images were captured with brightfield microscopy using the Zeiss Imager D1, connected to a Zeiss AxioCam MRc5 colour camera and using AxioVision 40 version 4.7.1.0 acquisition software (Zeiss, Germany) with 10 images per section, from 2 sections per heart. Image analysis was performed using Image Pro Plus (V4.5.1, Media Cybernetics, MD, USA) in a 'blinded' manner. Briefly, images were converted to grey scale (255 pixel range), a pixel intensity histogram was assessed to determine the non-biased threshold point of collagen staining at 10% above the inflexion point in the histogram distribution. A binary map of collagen deposition was generated, from which collagen density was calculated and expressed relative to the total number of pixels in the area of interest. For each section, ten images per section positioned reproducibly at septal and ventricular free wall locations were analysed. In some images discrete areas of focal fibrosis were apparent. For all images a value of total fibrosis (expressed % area) was determined and the mean value for all image fields calculated. For those images where discrete fibrotic foci were apparent, an additional determination of mean 'interstitial fibrosis' was made excluding these areas.

Cardiomyocyte Structural Analysis by Tissue Section Confocal Microscopy

For ultrastructural analysis to examine cardiomyocyte sarcomeric integrity, high resolution confocal microscopy was performed using fixed tissues labelled with the fluorescent marker wheat germ agglutinin (WGA, Alexa-594) to delineate cardiomyocyte T-tubule geometry as previously described.[6,7] Fluorescent images of labelled tissue sections were recorded with a Zeiss LSM410 confocal microscope using a Zeiss 63x NA 1.25 oil-immersion objective. Frequency analysis was used to assess the integrity of sarcolemmal T-tubular structure and the height of the peak at the sarcomere frequency of t-tubule labeling was used as one metric for integrity. The t-tubule images were converted to frequency space using the fast Fourier transform in the programming language IDL (Exelis). The height of the peak in the power spectrum corresponding to the sarcomere spacing (at ~0.5 µm-1) was then estimated by fitting a Gaussian ('T power').

Cell Isolation and Cardiomyocyte Morphology

Electromechanical performance of fura-2 loaded isolated cardiomyocytes obtained from HHR and NHR hearts at age ~30 weeks was evaluated (HHR 33.6±6.7 vs NHR 30.7±6.4 weeks), a timepoint selected as a disease progression stage immediately prior to emergence of premature mortality in HHR. NHR and HHR animals were weighed and then killed by decapitation under deep isoflurane anaesthesia. Hearts were blotted and wet heart weight measured. Single ventricular myocytes were isolated enzymatically using methods previously described.[5,8] Briefly, hearts were removed and perfused retrogradely on a Langendorff apparatus with Ca^{2+}-free bicarbonate-buffered physiological saline solution, maintained at 37°C, with the following composition (mM): NaCl, 118; KCl, 4.8; KH_2PO_4, 1.2; $MgSO_4$, 1.2; $NaHCO_3$, 25, glucose, 11. Following 20 minutes of 0.45 mg/ml collagenase (Worthington; Type II) perfusion, hearts were removed from the perfusion apparatus, the left ventricle was isolated, placed in a conical flask and myocytes were dispersed by gentle agitation. Fractions containing viable cells were re-suspended at room temperature in 2-3 mls of HEPES-buffered physiological saline containing 1mM Ca^{2+} and were stored at room temperature. Cells were used within 8 hours. From each heart, 100 rod-shaped and regularly striated cardiomyocytes were selected randomly for length and width measurement at × 400 magnification using a Nikon inverted light microscope and calibrated eye piece as previously described.[5,8] Cell volume was calculated from the product of cell length and cell width using the previously described relationship between these parameters,[9] in which cell volume is calculated as 7.59×10^{-3} pL/μm^2 × cell area (μm^2).

Whole-Cell Patch Clamp

I-Ca and I-NCX from NHR and HHR were measured in whole cell voltage clamp, using an Axopatch 200B patch-clamp amplifier (Axon Instruments, Foster City, CA) coupled to an A-D amplifier (Digidata 1200B, Axon Instruments) with 1-3 MΩ pipette resistances (glass type TW150F-3, World Precision Instruments, Sarasota, FL) as previously described.[10] Prior to I-Ca and I-NCX measurements, membrane capacitance (Cm) was calculated from 5 mV hyperpolarizing and depolarizing steps applied from holding potential of -90 mV.

For I-Ca measurements, the pipette contained (in mM): CsCl 100, TEA-Cl 20, MgATP 5, Li-GTP 0.2, EGTA 10, HEPES 10, and pH 7.4 adjusted with CsOH at room temperature (22-25°C). Cells were superfused with normal Tyrode's solution containing (mM): NaCl 140, KCl 6, D-glucose 10, HEPES 5, $MgCl_2$ 1, $CaCl_2$ 1, and pH 7.4 adjusted with NaOH at room temperature. Once a successful 'break in' was obtained, the perfusion medium was switched to the modified normal Tyrode's solution containing (mM): TEA-Cl 140, CsCl 6, to replace NaCl, KCl respectively and pH 7.4 adjusted with TEA-OH. Voltage step protocols with three holding potentials (HP) were applied to identify the calcium currents available at different potentials: -115 mV (all currents), -90 mV (substantially excluding $I\text{-}Ca_{(TTX)}$) and -50 mV substantially excluding both $I\text{-}Ca_{(T)}$ and $I\text{-}Ca_{(TTX)}$. At each HP, test pulses were 400 ms depolarization and were made at test voltages ranging up to +60 mV, with steps of +10 mV increments (the interval between pulses was 2 s).

For I-NCX measurements, the solutions were adapted from Pogwizd *et al.* 1999.[11] The pipettes contained CsCl 45, Cs methanesulfonic acid 55, ATP-tris 10, GTP-tris 0.3, $MgCl_2$ 10.8, NaCl 14, $CaCl_2$ 2.21 (100 nmol/L free Ca), 1,2-bis (2 amino phenoxy) ethane-N,N,N',N'-tetra acetic acid (BAPTA) 5, Di-Br-1,2-bis (2 amino phenoxy) ethane-N,N,N',N'-tetra acetic acid (Di-Br BAPTA) 5, HEPES 20. To isolate I-NCX the normal Tyrode's solution was modified (CsCl 6 to replace KCl, $CaCl_2$ 2, BDM 30 and strophanthidin 10 μmol/L to block Na/K-ATPase pump). To measure the I-NCX a combined voltage step and ramp protocol was applied.[11,12] From an initial holding potential (HP) of -90 mV, the cell was depolarized to -45 mV (400 ms) to activate and inactivate Na current. Then a step from -45 mV to 0 mV (200 ms) was used to activate and inactivate I-Ca. Finally, the voltage was stepped to +80 mV (200 ms) and ramped down to -140 mV (1000 ms) to assess I-NCX. The protocol was repeated in the presence of 5 mM $NiCl_2$ to obtain Ni-sensitive I-Ca and I-NCX. To isolate I-NCX, the current traces were subtracted and the residual current measured during the +80 mV to -140 mV ramp was identified as I-NCX. Current analysis and curve fitting procedures were performed using Clampfit in pClamp8. For calculation of current density, currents were normalized by Cm. Current analysis and curve fitting procedures were performed using Clampfit in pClamp8. For calculation of current density, currents were normalized by Cm.

Cardiomyocyte intracellular Ca^{2+} and Contractility Measurements

Intracellular Ca^{2+} and cell length were measured simultaneously by microfluorimetry and edge detection (Ionoptix MA, USA) as previously described.[13] Cells were loaded for 20 minutes with 2.5μM fura-2/AM (Molecular Probes, Eugene, Or, USA) at room temperature. They were placed in a chamber mounted on the stage of an Olympus IX51 inverted fluorescence microscope and superfused with 1.5 mM Ca^{2+} HEPES solution, 37°C at a rate of 2ml/min and stimulated to contract at 3Hz. Excitation light at 360nm and 380nm was provided by a 75-watt xenon lamp and filter wheel. Emitted fluorescence (510 nm) was recorded by a photomultiplier tube, with the output current converted to voltage and digitized for subsequent analysis using the interpolated numerator method. Background correction was undertaken at the completion of each cell recording and incorporated into analysis protocol. The following calcium parameters were measured: diastolic Ca^{2+}, systolic Ca^{2+}, amplitude of the Ca^{2+} transient and time constant of decay of the Ca^{2+} transient (tau). Phase-loop plots of single cardiomyocyte contraction cycles through shortening and lengthening were constructed to provide an indication of shift in cardiomyocyte Ca^{2+} sensitivity as previously described.[13] In a pilot experiment sarcoplasmic reticulum Ca^{2+} load level in myocytes immediately following steady state contraction was determined by rapid and brief exposure of myocytes to 10mM caffeine. The peak of the Ca^{2+} contracture transient generated through store discharge via opened SR Ca^{2+} release channels was measured.

Cell length was measured using an edge detection system under basal conditions. For each contraction cycle, a range of normalized contractile parameters was automatically computed and averaged (% shortening (%S), time to peak shortening (Tm), maximum rate of shortening (mrs), maximum rate of lengthening (mrl) and time to cycle completion (Tf)). Cardiomyocyte performance was evaluated: (i) under basal paced conditions (37°C, 3Hz, 1.5mM Ca^{2+}), (ii) during a rest interval (37°C, 1.5mM Ca^{2+} 3Hz for 5 mins, stimulator off 30 secs), and (iii) with different inotropic challenges (4 mM Ca^{2+}, isoproterenol 10^{-8}M). All data were analyzed off-line using IonWizard (IonOptix, Milton, MA, USA).

Immunoblotting

Hearts were isolated and the blood flushed from the coronary vasculature with cold Krebs-Henseleit bicarbonate buffer (4°C). Ventricles were rapidly removed and snap frozen in liquid nitrogen. Ventricles were homogenized in 100mmol/L Tris-HCl, pH 7.0, phosphatase inhibitors NaF and Na_3VO_4 (at 5mmol/L and 0.5mmol/L respectively), and chelators EGTA and EDTA at 5mmol/L each (10mL buffer/g tissue) using an Ultra-Turrax tissue grinder (Crown Scientific, NSW, Australia). Non-fractionated homogenates were reconstituted in sodium dodecylsulphate (SDS) sample buffer. Samples were normalized for protein content.

SDS-polyacrylamide gel electrophoresis (SDS-PAGE) was performed, as previously described,[14] using the Invitrogen XCell system (Invitrogen, VIC, Australia) using non-fractionated homogenate samples. After electrophoresis, proteins were transferred onto polyvinyl diflouride (PVDF) membranes using the XCell II blotter (Invitrogen, VIC, Australia). PVDF membranes were incubated in primary antibodies overnight at 4˚C. Membranes were subsequently probed with the appropriate secondary antibody for 1 hour at room temperature and incubated in enhanced chemiluminescent reagent (Amersham ECL Plus, GE Healthcare) for 5 minutes. Protein bands were visualized with a Bio-Rad Chemi-XRS Imaging device, and band intensity was quantified using Quantity One imaging software (Bio-Rad). Representative Coomassie stained membranes (Fig S1B), confirmed equal loading of protein across all lanes in multiple gels used for each protein evaluation. In addition, dual calibrator control samples were included for all gels for every protein evaluated. Primary antibodies used in this study are tabulated (Fig S1A). For titin detection, protein bands and total phospho-protein levels were visualized using protein gel stains (Table S3).

Statistical Analyses

In general (unless otherwise stated) data are presented as mean ± SEM. Sample sizes were estimated based on previous findings reported using similar techniques when possible. Comparisons between two groups with normally distributed data were performed with Student's unpaired t-test. Data from experiments with two groups assessed at multiple points were evaluated by a one-way analysis of variance (ANOVA) with repeated measures. Two-way ANOVA was used for evaluation of data groups comprising 2 factors. Correlation analyses were performed to determine the Pearson Coefficient within each strain and significance values evaluated. Data are shown depicting linear regression plots for each strain (SPSS c21.0; Graph Pad Prism V6). Data analysis was performed in a blinded manner. Survival (Kaplan Meier) data were analyzed by Log-rank Mantel-Cox test. Differences were considered significant at $P < 0.05$ (SPSS v.21.0; Graph Pad Prism V6).

Table S1. Echocardiographic and hemodynamic (cardiac catheterization) analysis of 50 week and 30 week HHR and NHR hearts.

Parameter		50 weeks		30 weeks	
		NHR	HHR	NHR	HHR
Echocardiography					
IVSd	(mm)	1.71 ± 0.04	2.20 ± 0.13*	1.76 ± 0.02	2.21 ± 0.06*
LVPWd	(mm)	1.89 ± 0.05	2.47 ± 0.23*	1.83 ± 0.08	2.62 ± 0.13*
LVIDd	(mm)	8.39 ± 0.12	9.21 ± 0.48	7.76 ± 0.12	8.87 ± 0.54
LVIDs	(mm)	5.01 ± 0.26	6.43 ± 0.36*	4.50 ± 0.20	5.96 ± 0.43*
FS	(%)	39.89 ± 2.2	30.35 ± 2.8*	42.14 ± 2.1	33.67 ± 1.1*
EF	(%)	74.6 ± 1.3	64.0 ± 3.8*	81.8 ± 1.6	73.2 ± 1.3*
HR	(bpm)	308 ± 6	352 ± 8*	312 ± 10	347 ± 7*
E wave velocity	(mm/s)	712 ± 54	1184 ± 121*	690 ± 34	1103 ± 65*
A wave velocity	(mm/s)	392 ± 23	885 ± 136*	383 ± 22	770 ± 87*
E/A ratio	(ratio)	1.86 ± 0.1	1.46 ± 0.14	1.83 ± 0.12	1.56 ± 0.14
MV Dec T	(ms)	61.1 ± 2.9	35.5 ± 4.5*	49.0 ± 3.8	26.8 ± 3.5*
E’ velocity	(mm/s)	43.4 ± 4.4	46.9 ± 10.6	44.5 ± 3.5	35.2 ± 5.2
E/E’	(ratio)	16.9 ± 0.7	32.5 ± 4.6*	16.3 ± 1.0	33.3 ± 2.4*
Hemodynamic					
LVEDP	(mmHg)	10.6 ± 2.0	8.8 ± 1.9	N/A	N/A
+ dP/dt	(mmHg/s)	6200 ± 528	7894 ± 478*	N/A	N/A
- dP/dt	(mmHg/s)	5048 ± 532	5751 ± 465	N/A	N/A

IVSd – normalized interventricular septum at diastole (BW adjusted), LVPWd – normalized left ventricular posterior wall at diastole (BW adjusted), LVIDd – left ventricular inner diameter at diastole, FS – fractional Shortening, EF – ejection fraction, HR – heart rate, MV DecT – mitral valve deceleration time, LVEDP – left ventricular end diastolic pressure, + dP/dt – maximal slope of the systolic pressure increment, - dP/dt – maximal slope of the diastolic pressure decrement. (*p<0.05, 2-way ANOVA HHR vs NHR strain effect, n = 6 -10 hearts/group)

Table S2. HHR & NHR Cardiac and cardiomyocyte morphology during progression to failure (30 weeks).

Parameter		NHR	HHR
CWI	(mg/g)	3.40±0.1 (39)	4.50±0.3* (34)
Myocyte Length	(mm)	132.5±0.99 (22)	163.1±2.3* (16)
Myocyte Width	(mm)	29.7±0.3 (22)	35.8±0.7* (16)
Myocyte Capacitance	(pF)	302.1±15.0 (18)	384.5±14.2* (16)
Myocyte Volume	(pL)	29.84±0.4 (22)	44.34±1.3* (16)

Significant elevation of cardiac weight and cardiac weight index in HHR, with increased cardiomyocyte size measured morphologically by dimensions, by computed volume and electrophysiologically (by capacitance). Calculated cardiomyocyte deficit of approx. 20% fewer cells/HHR heart (see Online Supplement regarding myocyte count calculation). (*p<0.05, Student's t-test, N hearts n parentheses, myocyte dimensions measured from mean n=50 cells per heart).

Table S3. Gel staining summary information.

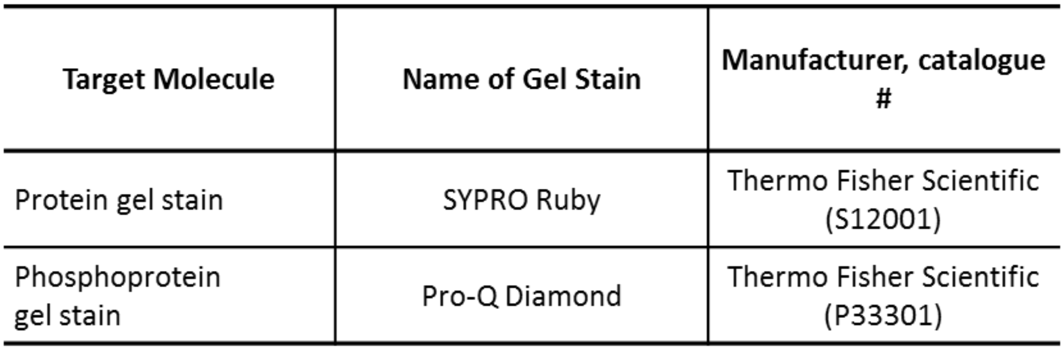

Target Molecule	Name of Gel Stain	Manufacturer, catalogue #
Protein gel stain	SYPRO Ruby	Thermo Fisher Scientific (S12001)
Phosphoprotein gel stain	Pro-Q Diamond	Thermo Fisher Scientific (P33301)

Figure S1. Telemetry blood pressure (20-30 weeks) and LV hemodynamic measurements (50 weeks).

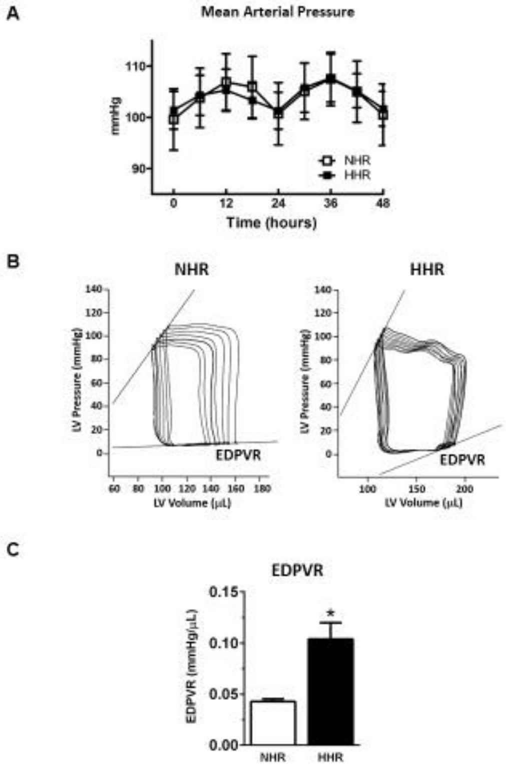

A. Equivalent (normotensive) diurnal mean arterial pressure (MAP) states in HHR and NHR. (mean ± SD, n=6 HHR and NHR, age 20-30 weeks). **B.** Representative Pressure-Volume loops in NHR and HHR. **C.** Mean End Diastolic Pressure-Volume Relationship (EDPVR) measurements in HHR and NHR. For Panels B & C graphs show mean ± SEM, n=8-9 HHR and NHR, age 50 weeks.

Figure S2. Immunoblot primary antibody summary information & Coomassie stained membranes.

A

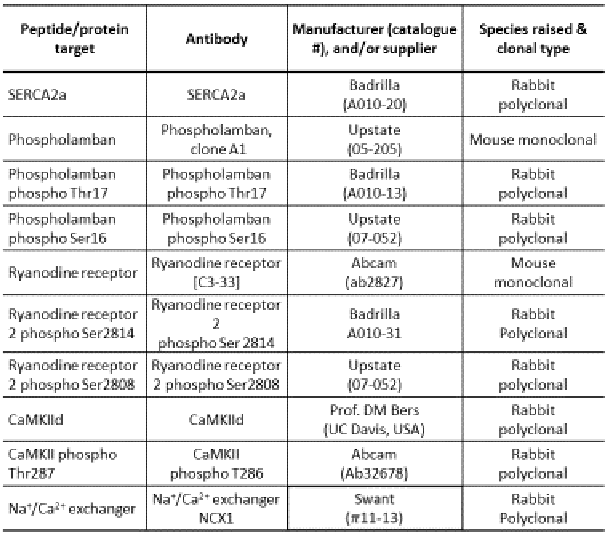

Peptide/protein target	Antibody	Manufacturer (catalogue #), and/or supplier	Species raised & clonal type
SERCA2a	SERCA2a	Badrilla (A010-20)	Rabbit polyclonal
Phospholamban	Phospholamban, clone A1	Upstate (05-205)	Mouse monoclonal
Phospholamban phospho Thr17	Phospholamban phospho Thr17	Badrilla (A010-13)	Rabbit polyclonal
Phospholamban phospho Ser16	Phospholamban phospho Ser16	Upstate (07-052)	Rabbit polyclonal
Ryanodine receptor	Ryanodine receptor [C3-33]	Abcam (ab2827)	Mouse monoclonal
Ryanodine receptor 2 phospho Ser2814	Ryanodine receptor 2 phospho Ser 2814	Badrilla A010-31	Rabbit Polyclonal
Ryanodine receptor 2 phospho Ser2808	Ryanodine receptor 2 phospho Ser2808	Upstate (07-052)	Rabbit polyclonal
CaMKIId	CaMKIId	Prof. DM Bers (UC Davis, USA)	Rabbit polyclonal
CaMKII phospho Thr287	CaMKII phospho T286	Abcam (Ab32678)	Rabbit polyclonal
Na^+/Ca^{2+} exchanger	Na^+/Ca^{2+} exchanger NCX1	Swant (π11-13)	Rabbit Polyclonal

B

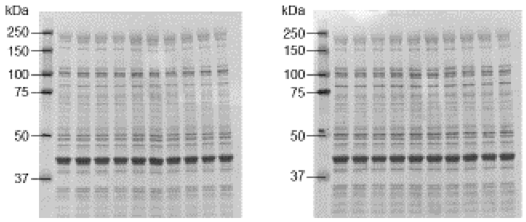

A. Immunoblot primary antibody summary information for HHR and NHR. **B.** Representative Coomassie stained membranes for HHR & NHR confirming equal loading of protein across all lanes.

Figure S3. Longitudinal systolic & diastolic NHR & HHR functional measurements.

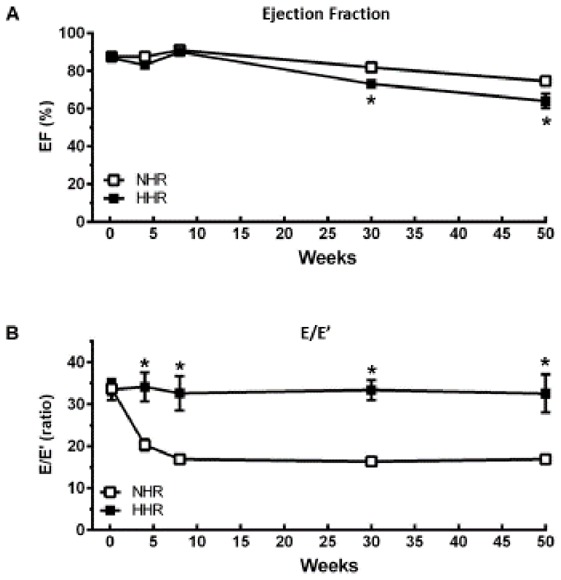

A. Mean changes in ejection fraction over 50 wks for HHR and NHR. **B.** Mean values for diastolic function ratio E/E’ over 50 wks in HHR and NHR. (n=6-14 HHR and NHR, mean ± SEM)

Figure S4. Locational fibrotic mapping of HHR cardiac transverse sections (age 50 weeks).

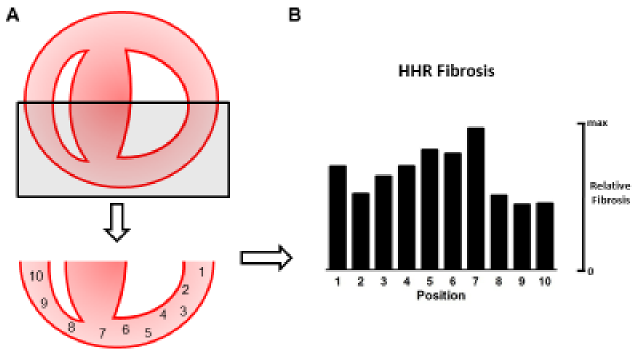

A. Schematic of transverse cardiac section indicating location of 10 image fields utilized for picrosirius analysis for all hearts. **B.** Mean relative fibrosis values from each of the ten locations, indicating more pronounced fibrosis at locations at/near position 7 and at position 1. (10 images per section, 2 sections per heart, N=5 hearts/group).

Figure S5. Titin-isoform composition and titin phosphorylation are unchanged in HHR (age 50 weeks).

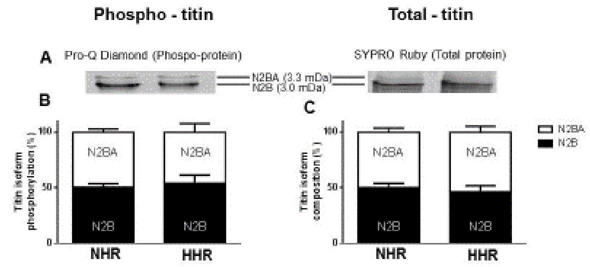

A. Representative immunoblot analyses of titin protein expression and phosphorylation levels from HHR and NHR left ventricular tissues. **B.** Titin isoform composition is not different between HHR and NHR. **C.** Total titin protein expression levels are not different between HHR and NHR (N=5 hearts/group).

Figure S6. Enhanced sarcolemmal Ca^{2+} current density in HHR vs NHR.

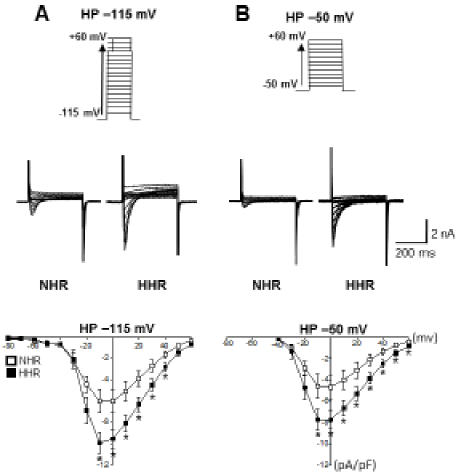

Voltage clamp protocol schematics, representative I-Ca current traces and mean normalized current-voltage plots obtained for voltage step protocols from two holding potentials (HP): **A.** HP-115mV; **B.** HP-50mV. Mean current densities (pA/pF) were significantly higher in the HHR at all holding potentials. (*p<0.05, 1-way ANOVA with repeated measures, n=12-18 cells/group). Graphs show mean±SEM, age 20-30 weeks (pre-failure).

Figure S7. NCX1 protein expression is unchanged in HHR (age 20-30 weeks).

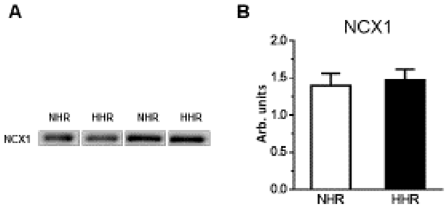

A. Representative immunoblot analyses of NCX1 protein expression from HHR and NHR left ventricular tissues. **B.** NCX1 protein expression is not different between HHR and NHR. (*$p<0.05$, Student's t-test. N=10 hearts/group). Graphs show mean±SEM.

Figure S8. NHR & HHR ECG parameters (age 50 weeks).

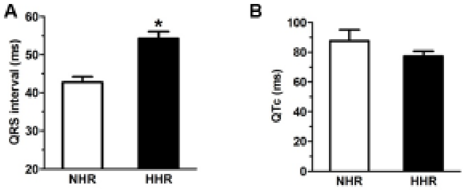

A. Mean QRS interval significantly extended in HHR. **B.** Mean QTc interval not different in HHR. (*p<0.05, Student's t-test. N=8-12 sample periods/heart, duration 10 sec). Graphs show mean±SEM.

Figure S9. Increased cardiomyocyte SR Ca^{2+} load in HHR.

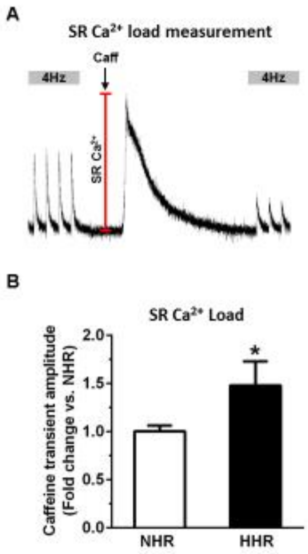

A. SR load measurement protocol using caffeine (10mM) induced Ca2+ release preceded by 4Hz steady state stimulation. **B.** Caffeine transient amplitude expressed as mean fold change. (*$p<0.05$, Student's t-test, n=10-20 cells, for N = 2-3 hearts, mean±SEM).

Supplemental References:

1. Harrap SB, Danes VR, Ellis JA, Griffiths CD, Jones EF, Delbridge LM. The hypertrophic heart rat: A new normotensive model of genetic cardiac and cardiomyocyte hypertrophy. *Physiol Genomics*. 2002;9:43-48.

2. Innes BA, McLauglin MG, Kapuscinski MK, Jacob HJ, Harrap SB: Independent genetic susceptibility to cardiac hypertrophy in inherited hypertension. *Hypertension* 1998;31:741-746.

3. Prestes PR, Marques FZ, Lopez-Campos G, Booth SA, McGlynn M, Lewandowski P, Delbridge LM, Harrap SB, Charchar FJTripartite motif-containing 55 identified as functional candidate for spontaneous cardiac hypertrophy in the rat locus cardiac mass 22. *J Hypertens*. 2016;34:950-8.

4. Zhang Y, Elsik M, Edgley AJ, Cox AJ, Kompa AR, Wang B, Tan CY, Khong FL, Stapleton DI, Zammit S, Williams SJ, Gilbert RE, Krum H, Kelly DJ. A new anti-fibrotic drug attenuates cardiac remodeling and systolic dysfunction following experimental myocardial infarction. *Int J Cardiol*. 201;168:1174-85.

5. Mellor KM, Bell JR, Young MJ, Ritchie RH, Delbridge LM. Myocardial autophagy activation and suppressed survival signaling is associated with insulin resistance in fructose-fed mice. *J Mol Cell Cardiol*. 2011;50:1035-1043.

6. Crossman DJ, Ruygrok PN, Soeller C, Cannell MB. Changes in the organization of excitation-contraction coupling structures in failing human heart. *PLoS One*. 2011;6:e17901.

7. Song LS, Sobie EA, McCulle S, Lederer WJ, Balke CW, Cheng H. Orphaned ryanodine receptors in the failing heart. *Proc Natl Acad Sci U S A*. 2006;103:4305-4310.

8. Domenighetti AA, Danes VR, Curl CL, Favaloro JM, Proietto J, Delbridge LM. Targeted glut-4 deficiency in the heart induces cardiomyocyte hypertrophy and impaired contractility linked with Ca^{2+} and proton flux dysregulation. *J Mol Cell Cardiol*. 2010;48:663-672.

9. Satoh H, Delbridge LM, Blatter LA, Bers DM. Surface:Volume relationship in cardiac myocytes studied with confocal microscopy and membrane capacitance measurements: Species-dependence and developmental effects. *Biophys J*. 1996;70:1494-1504.

10. Delbridge LM, Satoh H, Yuan W, Bassani JW, Qi M, Ginsburg KS, Samarel AM, Bers DM. Cardiac myocyte volume, Ca^{2+} fluxes, and sarcoplasmic reticulum loading in pressure-overload hypertrophy. *Am J Physiol*. 1997;272:H2425-2435.

11. Pogwizd SM, Qi M, Yuan W, Samarel AM, Bers DM. Upregulation of Na^{+}/Ca^{2+} exchanger expression and function in an arrhythmogenic rabbit model of heart failure. *Circ Res*. 1999;85:1009-1019.

12. Hobai IA, Bates JA, Howarth FC, Levi AJ. Inhibition by external Cd^{2+} of Na/Ca exchange and l-type Ca channel in rabbit ventricular myocytes. *Am J Physiol*. 1997;272:H2164-2172.

13. Mellor KM, Wendt IR, Ritchie RH, Delbridge LMD. Fructose diet treatment in mice induces fundamental disturbance of cardiomyocyte Ca^{2+} handling and myofilament responsiveness *Am. J. Physiol. Heart Circ. Physiol*. 2012; 302:H964-972.

14. Bell JR, Porrello ER, Huggins CE, Harrap SB, Delbridge LM. The intrinsic resistance of female hearts to an ischemic insult is abrogated in primary cardiac hypertrophy. *Am J Physiol Heart Circ Physiol*. 2008;294:H1514-1522.